



TechBriefs

National Aeronautics and
Space Administration



Electronic Components and Circuits



Electronic Systems



Physical Sciences



Materials



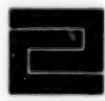
Computer Programs



Mechanics



Machinery



Fabrication Technology



Mathematics and Information Sciences



Life Sciences

98-09

99-006711

COMPLETED

September 1998

no

INTRODUCTION

Tech Briefs are short announcements of new technology derived from the research and development activities of the National Aeronautics and Space Administration. These Briefs emphasize information considered likely to be transferable across industrial, regional, or disciplinary lines and are issued to encourage commercial application.

Availability of NASA Tech Briefs and TSP's

Distribution of NASA Tech Briefs, a monthly periodical publication, is limited to engineers in U.S. Industry and to other domestic technology transfer agents. Requests for individual Tech Briefs or for Technical Support Packages (TSP's) announced herein should be addressed to

NASA Center for AeroSpace Information
Technology Transfer Office
800 Elkrige Landing Rd.
Linthicum Heights, MD 21090-2934
Telephone No. (301) 621-0245

Please reference the three-letter, five-digit control number located at the end of each Tech Brief. Information on NASA's Technology Utilization Program, its documents, and services is also available at the same facility.

Technology Utilization Officers and Patent Counsels are located at NASA field installations to provide technology-transfer access to industrial users. Inquiries can be made by writing to NASA field installations listed below.

Technology Utilization Officers and Patent Counsels

Ames Research Center
Technology Utilization Officer
Mail Code 223-3
Moffett Field, CA 94035

Patent Counsel
Mail Code 200-11
Moffett Field, CA 94035

Goddard Space Flight Center
Technology Utilization Officer
Mail Code 702-1
Greenbelt, MD 20771

Patent Counsel
Mail Code 204
Greenbelt, MD 20771

Lyndon B. Johnson Space Center
Technology Utilization Officer
Mail Code IC-4
Houston, TX 77058

Patent Counsel
Mail Code AL3
Houston, TX 77058

John F. Kennedy Space Center
Technology Utilization Officer
Mail Stop PT-PMO-A
Kennedy Space Center, FL 32899

Patent Counsel
Mail Code PT-PAT
Kennedy Space Center, FL 32899

Langley Research Center
Technology Utilization Officer
Mail Stop 143
Hampton, VA 23665

Patent Counsel
Mail Code 279
Hampton, VA 23665

Levi's Research Center
Technology Utilization Officer
Mail Stop 7-3
21000 Brookpark Road
Cleveland, OH 44135

Patent Counsel
Mail Code LE-LAW
21000 Brookpark Road
Cleveland, OH 44135

Jet Propulsion Laboratory
Technology Utilization Officer
Mail Stop 156-211
4800 Oak Grove Drive
Pasadena, CA 91109

NASA Resident Office-JPL
Technology Utilization Officer
Mail Stop 180-801
4800 Oak Grove Drive
Pasadena, CA 91109

Patent Counsel
Mail Code 180-801
4800 Oak Grove Drive
Pasadena, CA 91109

George C. Marshall Space Flight Center
Technology Utilization Officer
Code AT01
Marshall Space Flight Center,
AL 35812

Patent Counsel
Mail Code CC01
Marshall Space Flight Center,
AL 35812

John C. Stennis Space Center
Technology Utilization Officer
Code HA-30
Stennis Space Center, MS 39529

NASA Headquarters
Technology Utilization Officer
Code CU
Washington, DC 20546

Assistant General
Counsel for Patent Matters
Code GP
Washington, DC 20546

Dryden Flight Research Center
Technology Utilization Officer
M/S D21-31
Bldg. 4832 Whse 7
Lilly Dr.
Edwards, CA 93523



National Aeronautics and
Space Administration

5 Electronic Components and Circuits



13 Electronic Systems



21 Physical Sciences



29 Materials



33 Computer Programs



37 Mechanics



43 Machinery



51 Mathematics and Information Sciences



This document was prepared under the sponsorship of the National Aeronautics and Space Administration. Neither the United States Government nor any person acting on behalf of the United States Government assumes any liability resulting from the use of the information contained in this document, or warrants that such use will be free from privately owned rights.

BLANK PAGE



Electronic Components and Circuits

Hardware, Techniques, and Processes

- 7 Fabrication of Thinned QWIP Arrays for Improved Performance
- 8 Bound-to-Quasi-Bound Quantum-Well Infrared Photodetectors
- 9 Optoelectronic Generation of Optical and Microwave Signals
- 10 Ultrathin Packaging of Multiple Integrated-Circuit Chips
- 11 Signal Preprocessor for Determining Time of Arrival

BLANK PAGE

Fabrication of Thinned QWIP Arrays for Improved Performance

Dark current and crosstalk would be reduced.

NASA's Jet Propulsion Laboratory,
Pasadena, California

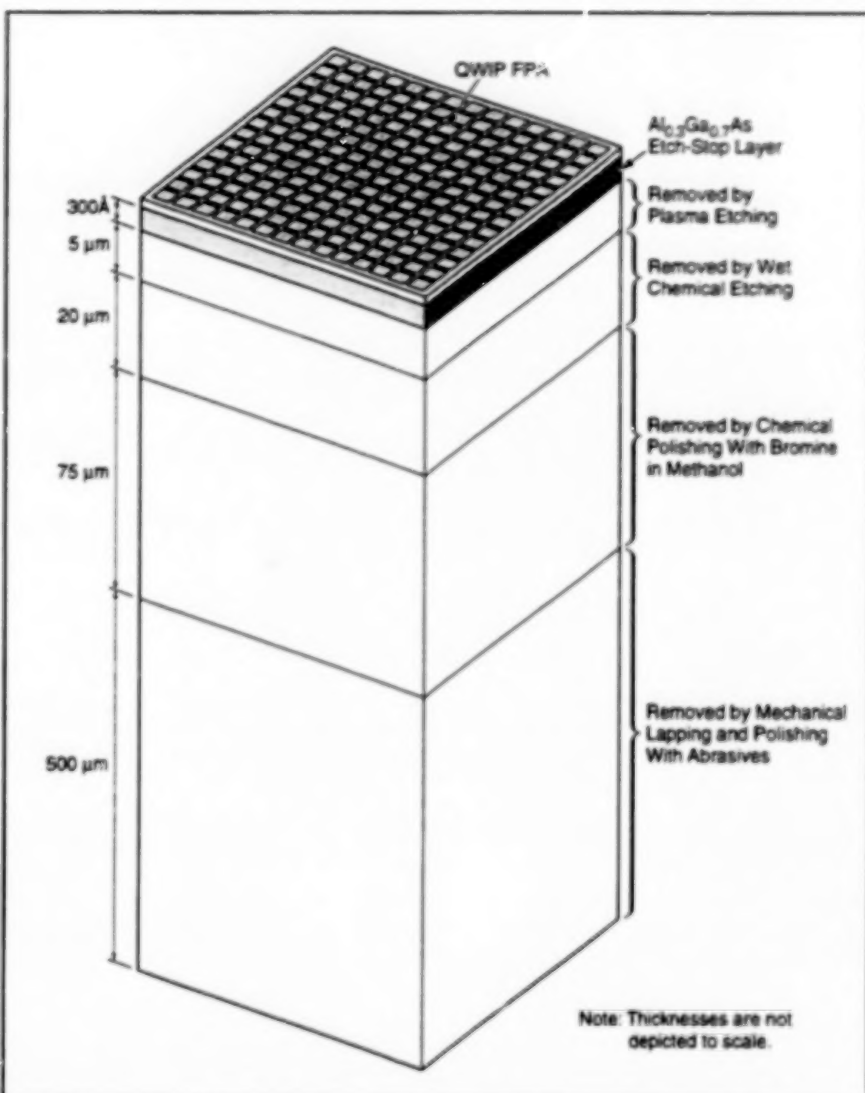
Focal-plane-array (FPA) hybrids of quantum-well infrared photodetectors (QWIPs) thinned to the membrane level are undergoing development. The developmental QWIPs in question are of the kind that exploit bound-to-quasi-bound absorption, as described, for example, in "Bound-to-Quasi-Bound Quantum-Well Infrared Photodetectors (NPO-19633), page 8. The present development encompasses both the thinned-array design and the method of fabrication.

Unthinned and partially thinned QWIP FPA hybrids developed previously have been characterized by crosstalk among pixels, thermal mismatches between the FPA hybrids and associated readout multiplexers, and poor light-coupling efficiency. The developmental thinned QWIP FPAs overcome these deficiencies and offer other improvements in performance, as follows:

- The thermal masses of FPAs are so small that they adapt the thermal expansion and contraction coefficients of Si CMOS (complementary metal oxide/semiconductor) readout multiplexers.
- The more favorable aspect ratios created by thinning maximize the efficiency of coupling of light from random reflectors.
- Crosstalk among pixels is suppressed because after thinning, the remaining substrate thickness is too small to support appreciable crosstalk.

A QWIP FPA of the present type is fabricated on top of a 300-Å-thick layer of $\text{Al}_{0.3}\text{Ga}_{0.7}\text{As}$ that, in turn, has been deposited on a relatively thick (several hundred μm) GaAs substrate. Then the thinned QWIP FPA is formed by removing the substrate from under the $\text{Al}_{0.3}\text{Ga}_{0.7}\text{As}$ layer in the following sequence of processes:

1. Formation of a QWIP FPA hybrid via indium bump-bonding process. This hybrid consists of QWIP FPA and Si CMOS readout multiplexer.
2. The hybrid is backfilled with low-viscosity epoxy.
3. By mechanical lapping and polishing with abrasives, most of the thickness is removed from the bottom side, leaving a substrate thickness of 100 μm .
4. Chemical polishing with a solution of 1 part bromine and 100 parts methanol is used to remove the next 75 μm .
5. The next 20 μm of thickness is removed in an 8-minute wet-chemical



The GaAs Substrate supports the QWIP FPA during initial fabrication. The substrate is removed by a sequence of processes, leaving only the QWIP FPA on the etch-stop layer.

6. The remaining 5 μm of substrate thickness is removed by dry etching in a plasma formed from CCl_2F_2 gas. The $\text{Al}_{0.3}\text{Ga}_{0.7}\text{As}$ layer acts as an etch-stop layer during this process, in that the plasma etches the GaAs substrate material much faster than it etches $\text{Al}_{0.3}\text{Ga}_{0.7}\text{As}$.
7. An O_2 plasma is used to remove a grayish film that remains after the CCl_2F_2 plasma etch.

This work was done by Sarath Gunapala, John K. Liu, and Mani Sundaram of Caltech for NASA's Jet Propulsion Laboratory. Further information

is contained in a TSP [see page 1].

In accordance with Public Law 96-517, the contractor has elected to retain title to this invention. Inquiries concerning rights for its commercial use should be addressed to

Technology Reporting Office
JPL
Mail Stop 122-116
4800 Oak Grove Drive
Pasadena, CA 91109
(818) 354-2240

Refer to NPO-19833, volume and number of this NASA Tech Briefs issue, and the page number.

Bound-to-Quasi-Bound Quantum-Well Infrared Photodetectors

Dark current is reduced substantially.

NASA's Jet Propulsion Laboratory,
Pasadena, California

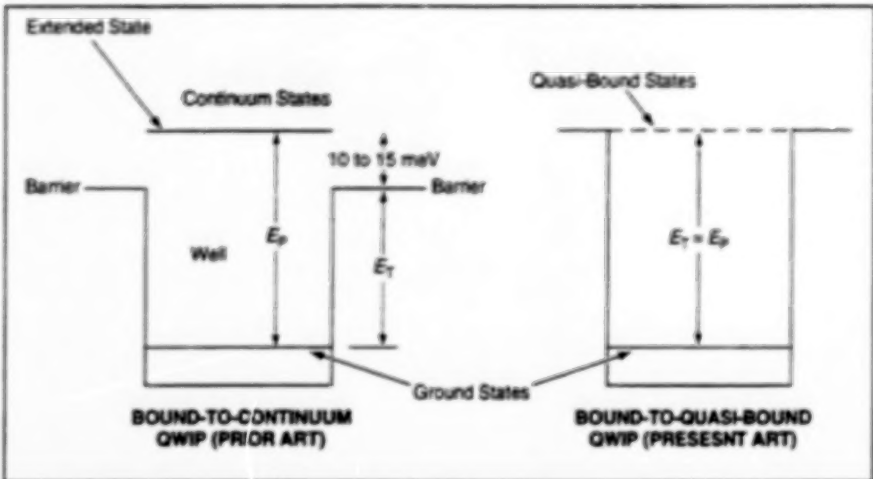


Figure 1. This Energy Diagram shows the differences between the quantum-well structures and quantum states in two types of QWIPs. In each case, E_p is the energy needed for intersubband photoionization and E_T is the energy needed for thermionic emission.

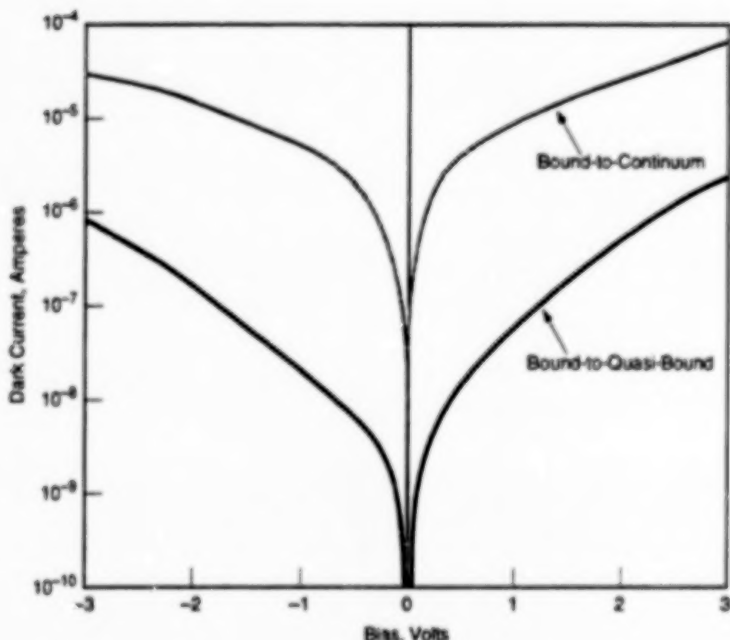


Figure 2. Dark Currents Were Measured in a bound-to-continuum and a bound-to-quasi-bound QWIP, each with area of $3.14 \times 10^{-4} \text{ cm}^2$, at a temperature of 55 K.

Multiple-quantum-well $\text{Al}_x\text{Ga}_{1-x}\text{As}$ photodetectors that exploit transitions of electrons from quantum-well bound states to quasi-bound states are undergoing development for use at wavelengths from 6 to 25 μm . These photodetectors are intended to provide detectivities that are higher (signal-to-noise ratios that are higher) than those of predecessor quantum-well infrared photodetectors that exploit

transitions of electrons from bound to continuum states.

Noise in a photodetector is associated with dark current — a component of current that flows whether or not illumination is present. The three mechanisms that contribute to dark current in a multiple-quantum-well photodetector are (1) temperature-independent quantum-mechanical sequential tunneling through

the barriers between the wells, (2) thermally assisted quantum-mechanical tunneling through the last barrier into continuum states, and (3) classical thermionic emission. The problem, then, is to maximize the photocurrent/dark-current ratio; this must be done by tailoring (a) the depth of the wells (by suitable choice of the composition parameter x in the well and barrier layers) and (b) widths of the wells and barriers (by suitable choice of the thicknesses of the well and barrier layers) to obtain a multiple-quantum-well structure that is optimum for the purpose.

In the development of the predecessor quantum-well infrared photodetectors (QWIPs), a large part of the strategy was to narrow the quantum wells to push the second bound quantum state (first excited state) into the continuum to obtain strong bound-to-continuum intersubband absorption. The major advantage of a bound-to-continuum QWIP is that a photoexcited electron can escape from a quantum well to the continuum transport states without having to tunnel through a barrier (see Figure 1). As a result, the bias needed to collect photoelectrons efficiently can be reduced from the bias needed to collect photoelectrons via quantum tunneling as in some prior photodetectors, thereby decreasing the component of dark current attributable to sequential quantum tunneling. Moreover, because the photoelectrons do not have to tunnel through the barriers, the barriers can be thickened to reduce ground-state sequential tunneling to effect a further decrease in dark current.

In a bound-to-continuum QWIP, the energy barrier, E_T , for thermionic emission is about 10 to 15 meV less than the energy, E_p , needed for intersubband photoionization; that is, the extended state (virtual level) lies 10 to 15 meV above the tops of the barriers between wells. A bound-to-quasi-bound QWIP (a device of the present type) differs from a bound-to-continuum QWIP in that the barriers are raised by 10 to 15 meV so that the first excited state lies at the tops of the barriers. The additional barrier height reduces thermionic emission over the barriers, thereby reducing the dark current. In addition, the bound-to-quasi-bound transition maximizes intersubband absorption while maintaining excellent electron transport.

As shown in Figure 2, the dark current

in an experimental bound-to-quasi-bound QWIP was found to be about 1/12 that of a comparable bound-to-continuum QWIP. As a result, the signal-to-noise ratio of the bound-to-quasi-bound device is about 3.5 times that of the bound-to-continuum device.

This work was done by Sarath D. Gunapala, Jin S. Park, Gabby Sarusi,

and John K. Liu of Caltech for NASA's Jet Propulsion Laboratory. Further information is contained in a TSP [see page 1].

In accordance with Public Law 96-517, the contractor has elected to retain title to this invention. Inquiries concerning rights for its commercial use should be addressed to

Technology Reporting Office

JPL

Mail Stop 122-116

4800 Oak Grove Drive

Pasadena, CA 91109

(818) 354-2240

Refer to NPO-19633, volume and number of this NASA Tech Briefs issue, and the page number.

Optoelectronic Generation of Optical and Microwave Signals

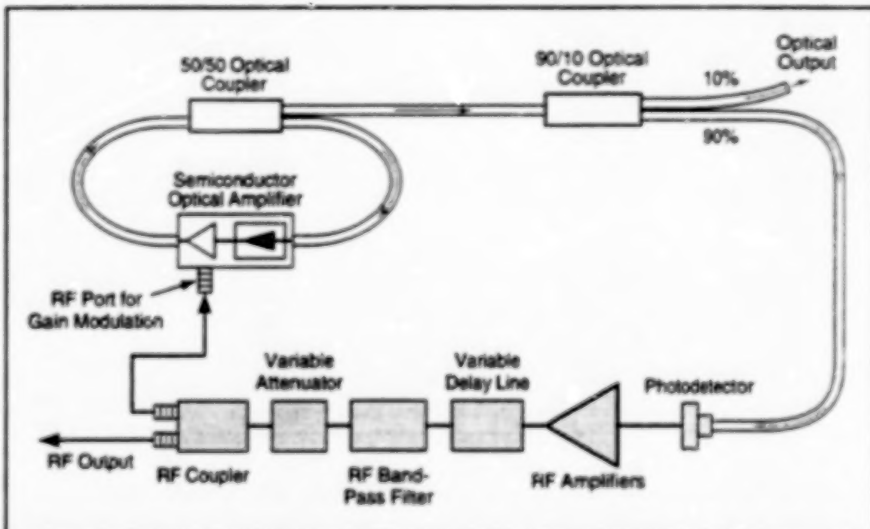
Optical and electrical oscillations are coupled to each other.

NASA's Jet Propulsion Laboratory,
Pasadena, California

The figure schematically illustrates an optoelectronic apparatus that generates both an optical output and an electronic output (typically at frequencies in the range from hundreds of megahertz to tens of gigahertz). The apparatus is denoted a "coupled opto-electronic oscillator" (COEO) because its optical and electronic oscillations are coupled to each other.

The COEO is the latest product of a continuing effort to develop photonic/electronic frequency synthesizers with low phase noise, wide tuning range, and high resolution in frequency. Previous developments in this effort were described in a number of articles in *NASA Tech Briefs*, including "Light Induced Microwave Oscillator" (NPO-19440), Vol. 20, No. 9 (September 1996), page 4a; "Electro-Optical Clock- and Carrier-Recovery Device" (NPO-19573), Vol. 20, No. 9 (September 1996), page 6a; and "Self-Injection-Locked Electro-Optical Microwave Oscillator" (NPO-19568), Vol. 20, No. 8 (August 1996), page 17a.

The COEO is based partly on concepts described in yet another prior *NASA Tech Briefs* article, namely, "Multiloop Photonic/Electronic Frequency Synthesizers" (NPO-19825), Vol. 21, No. 6 (June 1997), page 10a. To recapitulate: A rudimentary but impractical photonic/electronic oscillator would include a single optical feedback concatenated with an electrical feedback loop. By including a radio-frequency (RF) filter with narrow pass band in the electrical feedback loop, one could allow oscillations to occur in one electromagnetic mode while suppressing oscillations in other modes. To reduce phase noise, the length of the optical feedback loop must be increased; this would reduce the frequency interval between modes, necessitating a reduction in the bandwidth of the RF filter to ensure the selection of only the desired modal frequency. However, at a typical



This Coupled Opto-Electronic Oscillator generates stable microwave and pulsed optical outputs simultaneously.

frequency that one seeks to generate (of the order of 10 GHz), it is difficult to make an RF filter with pass band narrow enough to discriminate between modes. In addition, the inclusion of a narrow-band RF filter would sacrifice the tunability of the oscillator.

A multiple-loop apparatus could satisfy the need for both a longer optical feedback loop to reduce phase noise and a shorter optical feedback loop to facilitate discrimination against unwanted modes without need for a narrow-band RF filter, while providing broad frequency tunability. The multiple-loop apparatus proposed in the cited prior article would include a pump laser, a longer and a shorter fiber-optic delay line (longer and shorter optical feedback loops), a photodiode followed by an amplifier at the output end of each optical fiber, and a dual-drive electro-optical modulator that would be common to both fiber-optic delay lines and would be driven by the outputs of the amplifiers.

The COEO is a multiple-loop photonic/electronic oscillator, but it differs from the apparatus of the cited prior article in some important ways. Here, one does not use an external laser to pump the optoelectronic feedback loops; instead, the laser is an integral part of both the shorter feedback loop and of a semiconductor optical amplifier (SOA), the gain of which can be modulated electrically. The laser is a ring laser, so that its optical cavity (the ring) constitutes the shorter optical feedback loop. The laser has many longitudinal modes at integer multiples of a frequency interval that depends on the length of the loop. A typical value is 23.3 MHz, corresponding to a loop length of 8.58 m. The longitudinal modes of the longer loop are separated by much smaller frequency intervals.

A 50/50 optical coupler draws optical power from the shorter optical feedback loop, and a subsequent 90/10 optical coupler feeds optical power into the longer optical feedback loop. At other end of the

longer loop, the optical signal is fed to a photodetector. The electronic output of the photodetector is amplified, delayed, band-pass-filtered, and attenuated as needed, and some of the resulting RF signal is fed to the modulator port of the SOA.

The midband frequency of the band-pass filter is chosen to be an integer multiple of the frequency interval between laser modes, and the bandwidth is chosen to be less than this interval, so that the band-pass filter effectively picks out one of the beat frequencies between modes. Without the RF feedback to the SOA, the phases of the longitudinal modes of the ring laser would be independent of each other, so that the optical output would be nearly steady, with

superimposed random power fluctuations caused by interference among the modes. However, in the presence of the band-pass-filtered RF feedback at an integer multiple of the laser modal frequency interval, the sidebands of the modulated modes coincide with the frequencies of other modes, so that all the modes become injection-locked by the RF feedback. Many modes of the longer feedback loop compete to oscillate within the pass band, and the winner is the one with a frequency closest to the beat frequency, because only this one can mode-lock the ring laser. The superposition of locked modes causes the optical output to consist mostly of a train of pulses.

This work was done by Xiaofan Steve

Yao and Lutfollah Maleki of Caltech for NASA's Jet Propulsion Laboratory. Further information is contained in a TSP [see page 1].

In accordance with Public Law 96-517, the contractor has elected to retain title to this invention. Inquiries concerning rights for its commercial use should be addressed to

Technology Reporting Office

JPL

Mail Stop 122-116

4800 Oak Grove Drive

Pasadena, CA 91109

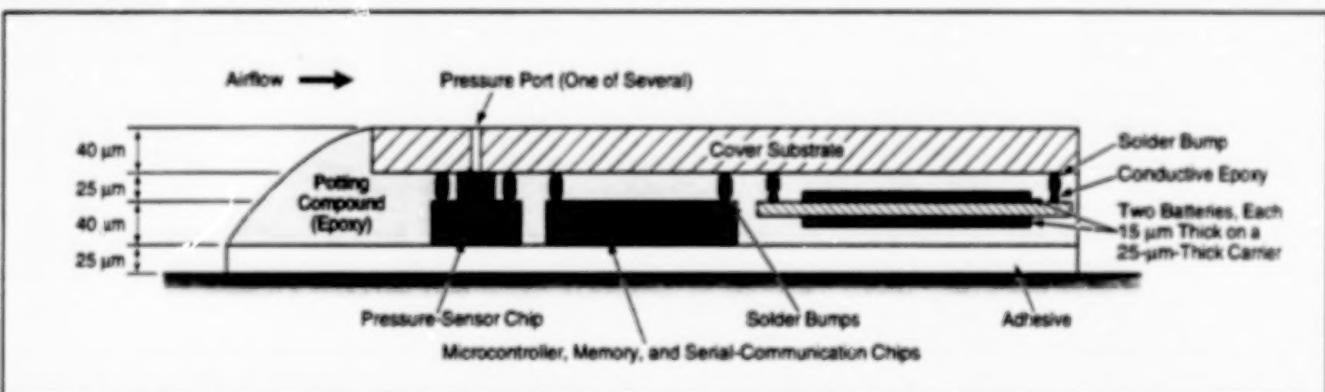
(818) 354-2240

Refer to NPO-20090, volume and number of this NASA Tech Briefs issue, and the page number.

Ultrathin Packaging of Multiple Integrated-Circuit Chips

An instrument package is only slightly thicker than a piece of paper.

Lewis Research Center,
Cleveland, Ohio



An instrument package that contains a pressure sensor and a data-acquisition system is so thin that it can be mounted on a surface exposed to a flow without appreciably perturbing the flow. For the sake of clarity, the thickness scale is greatly exaggerated in this view.

A process being developed for ultrathin packaging of multiple integrated-circuit chips and associated microelectromechanical components makes it possible to fabricate a minimally invasive pressure-measuring instrument to be used in characterizing a boundary-layer flow inside a turbomachine. Such an instrument must be thin enough not to appreciably perturb the flow; according to specifications supplied by NASA researchers, this means that the entire instrument package must be less than 5 mils (127 μm) thick. In comparison, a piece of copy paper is about 4 mils (102 μm) thick.

To achieve the needed capabilities for collection, storage, and processing of measurement data, it is necessary to integrate sensor, microcontroller, and memory chips into a single package. In addition to conforming to the stringent specification regard-

ing overall thickness, the packaging is required to provide mechanical and electrical connections for all of the chips and for a rechargeable battery, protect the electronic components on the chips, hermetically seal the battery, expose a pressure-sensor diaphragm while preventing exposure of electronic circuits to the environment, provide means for charging the battery, and enable communication between the microcontroller and external data-processing equipment. Moreover, the thermal limits of the components must not be exceeded during the packaging process.

The packaging process, being developed to satisfy the foregoing requirements, is a highly modified flip-chip process that involves a novel extension of conventional packaging techniques.

The figure presents a simplified cross section of the finished instrument package

adhesively bonded to a surface exposed to the flow to be measured, showing the battery and a few of the chips connected to the cover substrate. Note that the overall thickness of the package plus the adhesive is 130 μm, and could be reduced to less than the maximum allowable thickness of 127 μm by thinning the adhesive layer to 22 μm or less.

This work was done by Daniel A. Pruzan of Nielsen Engineering & Research for Lewis Research Center. Further information is contained in a TSP [see page 1].

Inquiries concerning rights for the commercial use of this invention should be addressed to NASA Lewis Research Center, Commercial Technology Office, Attn: Tech Brief Patent Status, Mail Stop 7-3, 21000 Brookpark Road, Cleveland, Ohio 44135. Refer to LEV-16545.

Signal Preprocessor for Determining Time of Arrival

A proposed analog/digital circuit would improve the accuracy of determining the time of occurrence of a peak in an analog waveform. In the past, the time of occurrence of the peak was determined by comparing the magnitude of digital data samples. The time or clock pulse associated with the peak magnitude was taken as the time of occurrence of the peak of the waveform. The new technique saves a series of data samples (7) prior to and after the sample with the largest amplitude. The set of data samples is saved and is used

with curve-fitting equations to estimate the time of the peak of the waveform. This can be done because of the deterministic character of the waveforms. This technique allows the time of occurrence of the peak of the waveform to be determined with greater resolution than can be obtained by simply sampling the data and looking for the peak. This technique has applications in systems where it is desirable to determine the relative time between waveforms. The Lightning Detection and Ranging (LDAR) system at KSC uses the differ-

ences in the time of arrival of lightning waveforms at seven sites, to locate lightning sources. The technique described is being implemented in the improved system to increase accuracy.

This work was done by Carl L. Lennon of Kennedy Space Center. Further information is contained in a TSP [see page 1].

Inquiries concerning rights for the commercial use of this invention should be addressed to the Patent Counsel, Kennedy Space Center; (407) 867-6225. Refer to KSC-11805.

BLANK PAGE



Electronic Systems

Hardware, Techniques, and Processes

- 15 Engine Monitoring Based on Normalized Vibration Spectra
- 16 Parallel-Processing CDMA Detector With Neural Network
- 17 Automated Cargo-Tracking Transponders
- 18 Switching Protocol for Optical Packet Data Communication
- 19 "Smart" Camera for Precise Mapping and Targeting

BLANK PAGE

Engine Monitoring Based on Normalized Vibration Spectra

Spectra are normalized in frequency and phase, then classified by a neural network.

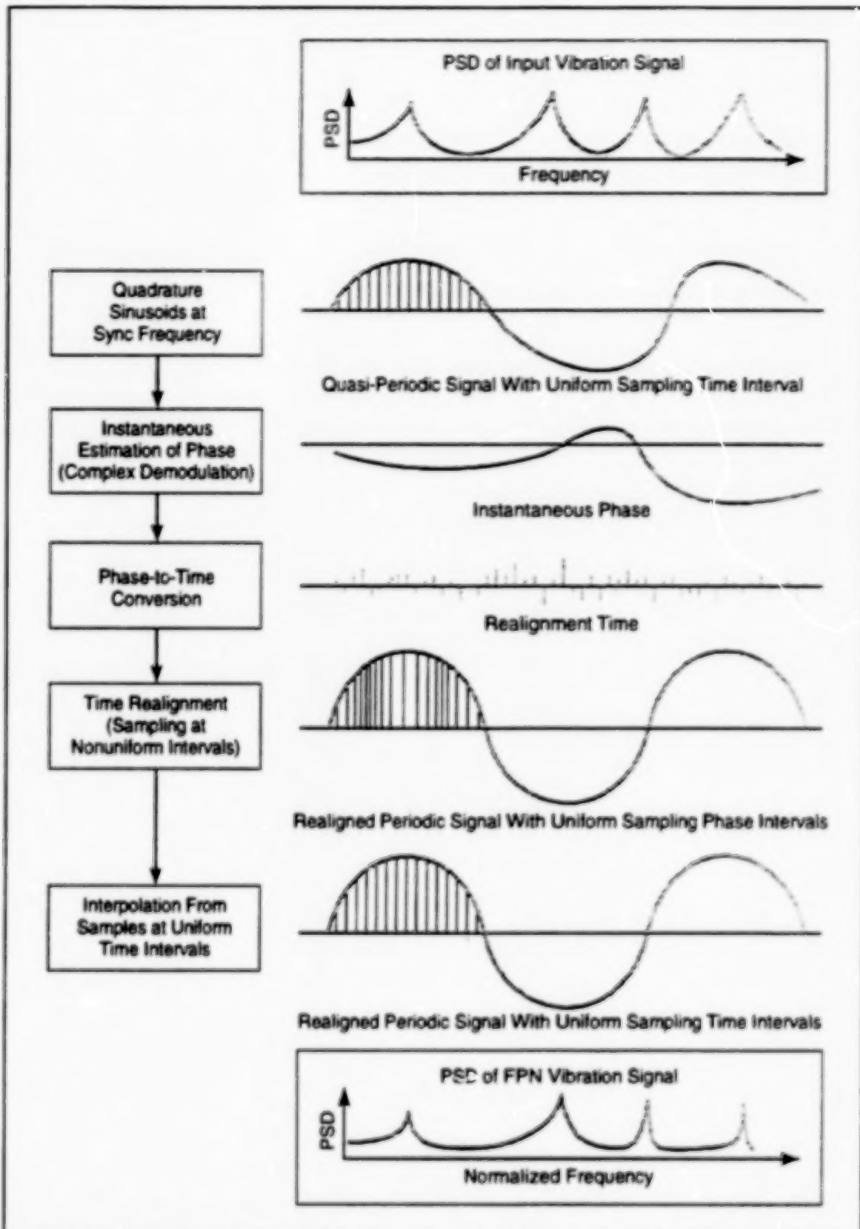
Marshall Space Flight Center,
Alabama

An electronic engine-health-monitoring system is based on (1) computation of frequency-phase-normalized (FPN) spectra from the digitized outputs of vibration sensors and (2) the use of these spectra as feature vectors, which are presented to an artificial neural network for recognition of features associated with incipient failures. The normalization in question is with respect to the instantaneous frequency and phase of rotation of the engine shaft [customarily denoted the "sync" (short for "synchronous") frequency and phase, respectively]. FPN spectra are useful for extracting that dynamical information that is most useful for detection and classification of failures.

Most machinery failures are preceded by growing tolerances, imbalances, and bearing-element wear, which give rise to subtle modifications of vibration waveforms. The vibration waveforms, and thus the subtle waveform modifications, are corrupted by such benign phenomena as environmental noise, fluid/structural interactions, nonlinear coupling, and feedthrough of vibrations from nearby machinery, all of which compound the diagnostic task. An important element of a vibration-based engine-monitoring system is the ability to extract true defect "signatures" from vibration-sensor outputs that also contain signatures of benign phenomena.

Other, similar systems have utilized frequency normalization; in particular, scaling of the frequency variables of conventional power spectral densities (PSDs) to sync frequencies, to provide more robust representations and simplify analyses of sync-related spectral components. However, the frequency-normalization processes in most such systems discard information on the relative phases of spectral components at various frequencies. These phase relationships are well hidden (they cannot be identified from conventional PSDs). They arise from nonlinear interactions among mechanical components; often, such nonlinear interactions are caused by mechanical defects. In the present system, the relative-phase information is preserved in the frequency-normalization process and is utilized to extract additional information about defects.

The raw vibration-sensor output is sampled and processed according to the phase-synchronized enhancement method (PSEM) (see figure). In this method, the



The **PSEM Algorithm** converts a quasi-periodic signal to a periodic signal in which sync-related components are at discrete frequencies.

quasi-periodic vibration signal is first sampled at constant time intervals. The sync component of the signal is assumed to be characterized by small fluctuations in frequency and phase about a constant, pure sync tone; the instantaneous sync frequency and phase fluctuations are obtained by applying a demodulation technique to quadrature sinusoid representations of the sync signal. The estimated phase fluctuations are converted to time fluctuations (realignment time) to obtain slightly nonuniform time intervals for resampling the vibra-

tion signal at uniform phase intervals. The uniform-phase samples are equivalent to uniform-time samples of constant-frequency sync and sync-related components. Once the sync frequency component becomes discrete in the resampled signal, all other sync-related components automatically become discrete.

The phase relationships of interest are those between the sync signal and its harmonics. These relationships can be quantified by use of a hyperspectrum that comprises a hierarchy of joint

moments between a reference spectral component (in this case, the sync component) and each of the harmonics. A hyperspectrum can be computed by use of fast Fourier transforms of signals that have been preprocessed by the PSEM.

The performance of the system has been studied in an application to vibration measurements from a bearing test rig, in

an effort to identify spectral signatures that could be correlated with wear marks on ball bearings. The results of the study thus far indicate that the inclusion of phase information in FPN spectra yields signatures that enable discrimination of subtle changes that are not represented by spectral energy density or amplitude alone. As a result, a neural network can

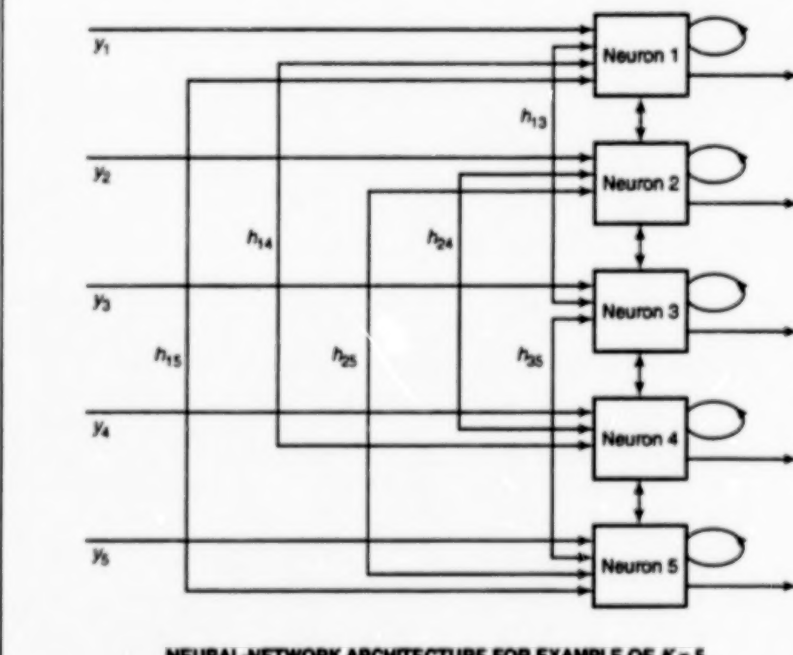
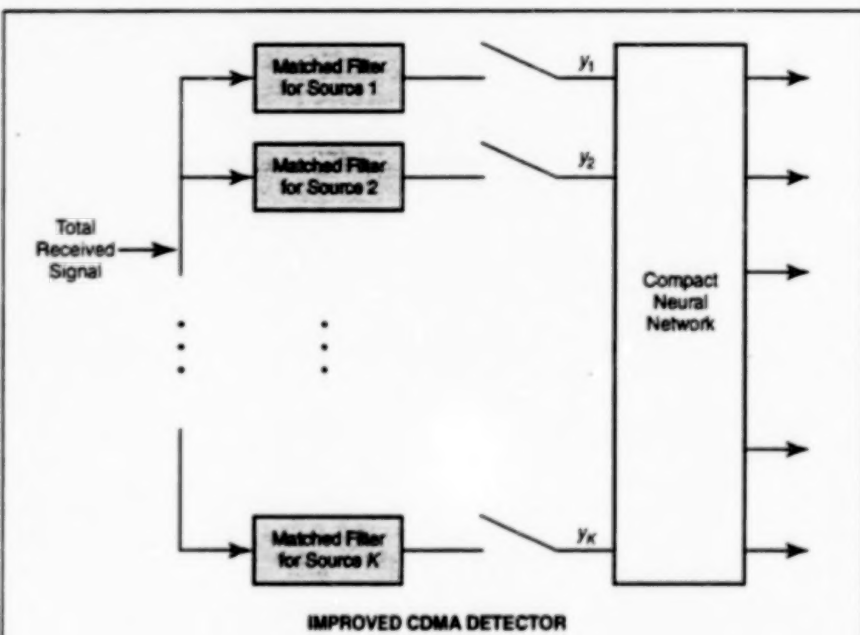
provide a more reliable and robust representation and classification of patterns for autonomous engine-health monitoring.

This work was done by Jong Jen-Yi of AI Signal Research, Inc., for Marshall Space Flight Center. Further information is contained in a TSP [see page 1].
MFS-2652G

Parallel-Processing CDMA Detector With Neural Network

Near/far resistance is achieved by solving an optimization problem.

NASA's Jet Propulsion Laboratory, Pasadena, California



A Compact Neural Network would process the outputs of matched filters in such a way as to obtain an optimal solution to the near/far problem.

A proposed improved code-division multiple-access (CDMA) detector would achieve high resistance to jamming of weak ("far") received signals by strong ("near") ones. The problem of such jamming is called the "near/far problem," and resistance to such jamming is called "near/far resistance." The near/far problem is a major technical obstacle in the operation of CDMA radio-communication systems; for example, a system in which a base station must communicate simultaneously with near and far mobile units.

In a CDMA system, the binary signal from each source is multiplied, before transmission, by a distinct pseudonoise-code or other signature waveform. In a conventional CDMA detector, the signal received from each of K sources is isolated from the other $K-1$ signals by use of one of K matched filters that function in parallel. In each matched filter, the total received signal is multiplied by the signature waveform for the source in question, and the resulting product is integrated in time over a symbol period. A simple decision device then chooses the received bit (+1 or -1) on the basis of the sign of the output of the matched filter.

The point of departure for the design of the improved CDMA detector was the observation that the near/far resistance of a CDMA detector could be maximized (in the sense that the probability of error in detected bits could be minimized) by minimizing a quadratic objective function. Given a tentative decision as to the signals received from the various sources and as to the bits that the signals represent during a symbol period, one suitable quadratic function is equivalent to an estimate of noise energy in the received signal.

The problem of minimizing an objective function amounts to an optimization problem. Thus, the near/far problem in CDMA reception can be converted to an optimization problem. A CDMA detector that

achieves near/far resistance by solving this optimization problem is called an "optimal multiuser detector" (OMD).

In the improved CDMA detector, the outputs of the matched filters would be fed to a parallel-processing, compact neural network (see figure) in which the synaptic weights would be based on the $K \times K$ matrix of cross-correlations of signature waveforms. The neural network would implement a gradient-descent algorithm in an effort to minimize an energy function that would be modified by addition of a constraint energy. A simulated-annealing technique called "hardware annealing" would be employed to escape

from local minima of the energy function. In the particular type of hardware annealing contemplated for this detector, the gain of each neuron would be continuously increased from a minimum to a maximum value. The combination of the constraint energy and the hardware annealing could significantly improve detection performance. A prototype very-large-scale integrated (VLSI) circuit version of the detector has been designed.

This work was done by Wai-Chi Fang of Caltech and Bing J. Sheu and Theodore W. Berger of USC for NASA's Jet Propulsion Laboratory. Further information is contained in a TSP [see page 1].

in accordance with Public Law 96-517, the contractor has elected to retain title to this invention. Inquiries concerning rights for its commercial use should be addressed to

Technology Reporting Office

JPL

Mail Stop 122-116

4800 Oak Grove Drive

Pasadena, CA 91109

(818) 354-2240

Refer to NPO-20205, volume and number of this NASA Tech Briefs issue, and the page number.

Automated Cargo-Tracking Transponders

Installed on cargo containers, these transponders could be interrogated from nearby or distant locations.

NASA's Jet Propulsion Laboratory,
Pasadena, California

Credit-card-sized electronic transponders have been proposed for use in tracking cargo anywhere on Earth. A transponder would be carried on a cargo container, where it would act as a "smart tag." The transponder would store data on the cargo in the container and would respond to inquiries — whether local or remote — about the contents and location of the shipment. The transponder and the communication and data-processing systems with which it would interact would ensure accurate and up-to-the-minute tracking of cargo, whether the cargo was in a warehouse, train, truck, airplane, or ship. Tracking cargo in this way would eliminate the need for the voluminous paperwork now used to track cargo and would make it unnecessary to prematurely open cargo containers at transshipment points to ascertain their contents.

A transponder would contain a microprocessor and a strip of random-access memory (RAM) integrated-circuit chips that would store the information on the cargo and its location. For limited applications, the transponder itself would be self-contained, with all the required functions [i.e., encoding, Global Positioning System (GPS), battery] retained by it. For universal applications, the transponder would be held in a retainer unit (see Figure 1) mounted on a cargo container. The retainer unit would be the medium through which information would be transferred. The retainer unit would function somewhat in the manner of a credit-card reader, except that the reading would be done completely electronically; that is, there would be no moving mag-

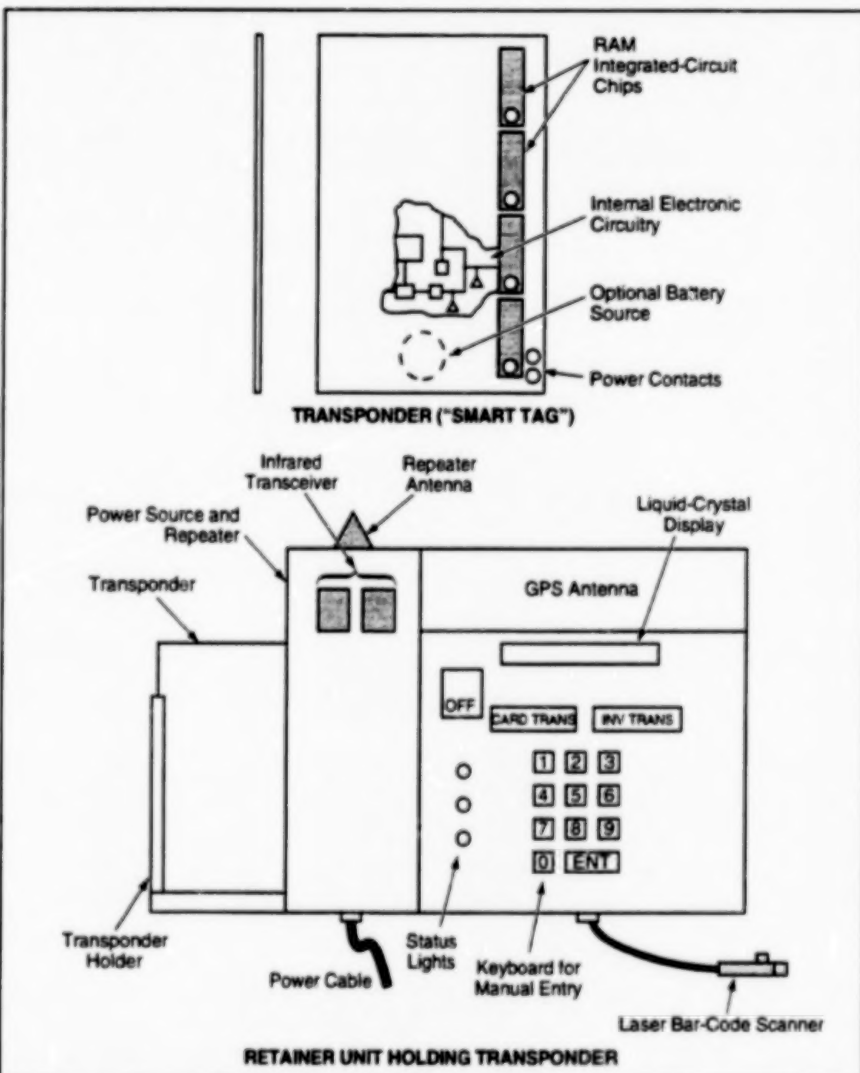


Figure 1. RAM Chips would be laid out in an area of about the same dimensions as those of the magnetic strip on a conventional credit card. The retainer unit would provide electric power (about 1 mW) to the transponder and would serve as an electrical interface between the transponder and the outside world. The retainer unit would be about the size of a hand calculator.

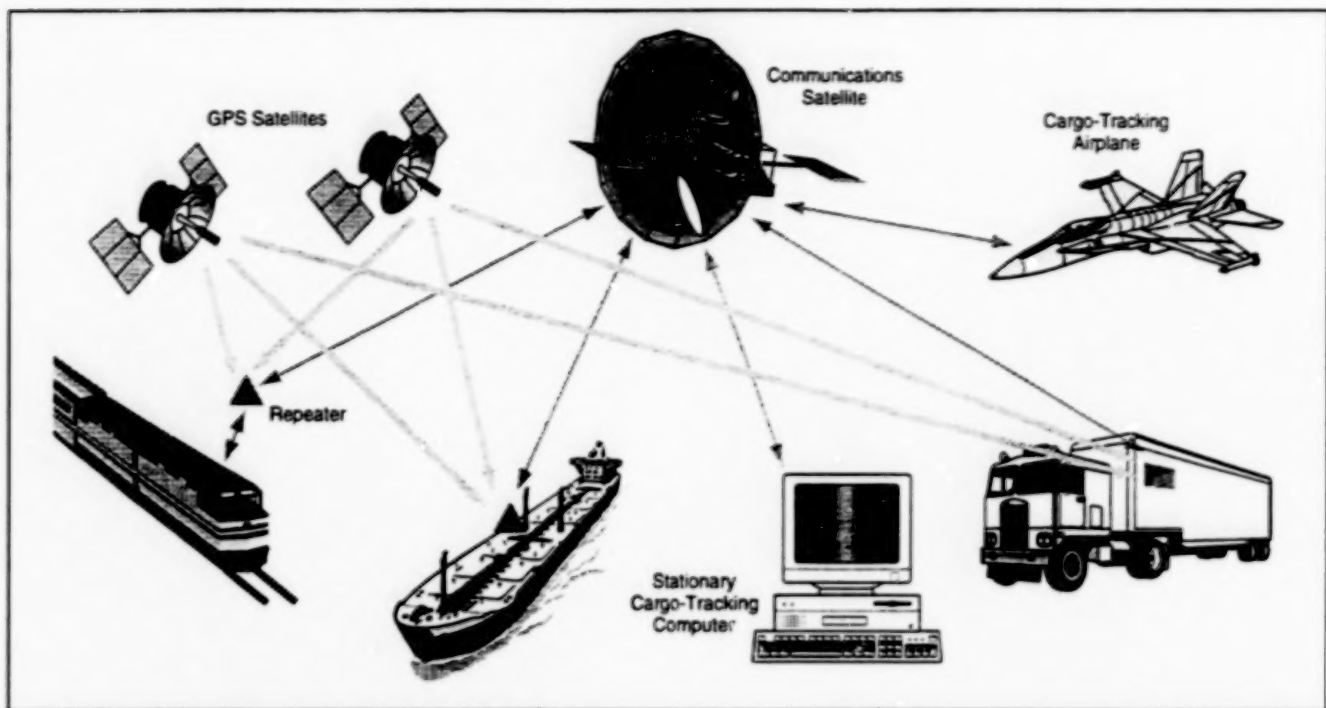


Figure 2. A Network of Satellites would link "smart" tags on transport vehicles over long distances to a central interrogation point. GPS satellites would send data to the tags about their current locations.

netic reader head because the information would not be stored in magnetic strips as it is on credit cards. The retainer unit would include an infrared transceiver for local communication and a microwave transceiver for communication over longer distances (see Figure 2).

There are many ways of transferring information to the transponder. Information on the cargo could be transferred into the transponder RAM from a laser bar-code scanner wired to the retainer unit by a long, flexible cord like a telephone cord. Alternatively, the information could be transmitted from a remote bar-code reader analogous to devices now used in rental-car-return yards. A third alternative would be to enter the data manually via a keyboard.

Either the transponder or the retainer unit would include a GPS receiver, with

GPS being integral with the transponder when used alone. Periodically (e.g., every 15 minutes) data on the latitude and longitude of the unit, as determined from GPS signals, would automatically be stored in the transponder RAM.

To retrieve information from the transponder at short range (about 100 m or less), an operator would aim an infrared interrogation "gun" at the retainer unit. From somewhat greater distances, information could be retrieved through infrared or microwave repeaters in the transport vehicle, at shipping depots, or at stations en route, for example. At still greater distances, satellite microwave links would be used. Thus, data on the contents, ownership, origin, destination, and location of a cargo container could be obtained at any time from anywhere.

When the cargo reached its destination, the transponder would be removed from the retainer and inserted into a reader on a personal computer to obtain a complete shipping record. The transponder could be then filed or reused for subsequent shipments.

This work was done by Philip J. Moynihan and Govind K. Deshpande of Caltech for NASA's Jet Propulsion Laboratory. Further information is contained in a TSP [see page 1].

This invention is owned by NASA, and a patent application has been filed. Inquiries concerning nonexclusive or exclusive license for its commercial development should be addressed to the Patent Counsel, NASA Resident Office-JPL [see page 1]. Refer to NPO-19769.

Switching Protocol for Optical Packet Data Communication

Multiple copies of headers would eliminate the need for storage of packets.

The figure illustrates aspects of a proposed switching protocol for optical packet data communication that would serve as an alternative to the older store-and-forward and header-first protocols. In both older protocols, it is necessary to store a single header from each packet of data

during the relatively long optical-switching time (typically tens of milliseconds) needed to set up optical input and output paths within each node. In the store-and-forward protocol, there is also a need for electronic storage of the data proper at each node during the setup time. Furthermore, typical

NASA's Jet Propulsion Laboratory, Pasadena, California

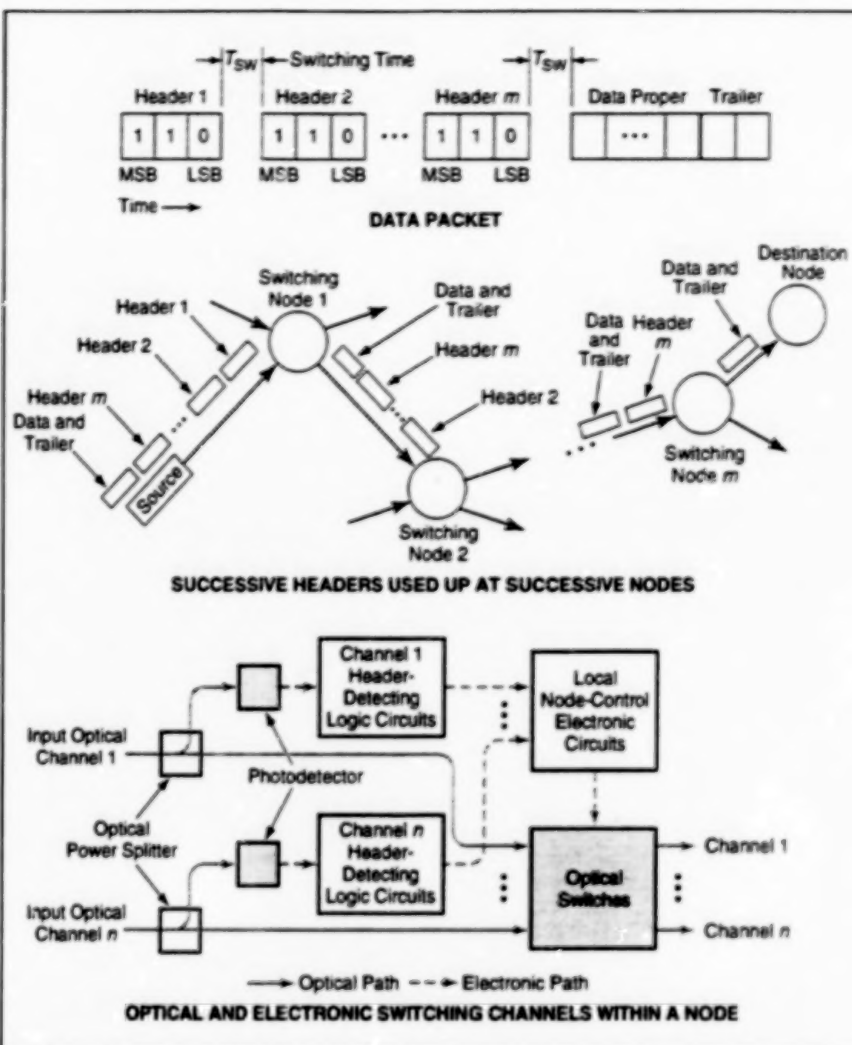
implementations of both older protocols have depended on electronic control circuitry between nodes to set up the optical paths between nodes.

The proposed protocol would eliminate the need for both (1) electronic storage of headers and data proper and (2) internode

electronic control circuitry. Depending on the specific implementation, local electronic control and switching circuitry might still be needed within each node, but the destination node address needed to set up the optical paths between nodes would be transmitted optically. Each data packet would begin with m identical copies of a header, where $m =$ the number of optical switches along the intended data path. Each copy of the header would contain the address of the destination node. The data proper would follow the headers and would be followed by a trailer.

Starting with the first copy of the header in a packet and working back along the packet, successive copies of the header would be consumed in setting up the optical switches within successive nodes along the path. The interval between successive copies of the header would be made long enough to allow sufficient time for optical switching to occur, in the foremost node along the path, in response to the first copy of the header to arrive there. By the time the second copy of the header had arrived at the foremost node along the path, the foremost node would be configured to transmit the header, along with the rest of the packet, to the next node. Thus, the second copy of the header to arrive at a node would be passed on to the next node, becoming the first copy to arrive there. This process would be repeated, each successive node along the path momentarily becoming the foremost node, until all m copies of the header were used up and the optical path through all m switching nodes was established. The data proper would then follow along the path, followed by the trailer. As it passed through each node along the path, the trailer would signal each node to break the optical path and await the arrival of the next header, if any.

Because of the long optical-switching times, the data in the headers could be transmitted at relatively low rates,



Each Copy of the Header Would Blaze the Trail for the next copy to go on to the next node and would be used up in the process. Enough copies (m) of the header would be provided so that the data packet could find its way to the destination node after traveling through m switching nodes.

enabling the use of correspondingly slow logic circuits within the nodes to detect headers and control the optical-switching functions. However, the data proper could still be transmitted at high rates (gigabits per second) because the data path would be all-optical.

This work was done by Steve P. Monacos of Caltech for NASA's Jet

Propulsion Laboratory. Further information is contained in a TSP [see page 1].

This invention is owned by NASA, and a patent application has been filed. Inquiries concerning nonexclusive or exclusive license for its commercial development should be addressed to the Patent Counsel, NASA Resident Office-JPL [see page 1]. Refer to NPO-19522.

"Smart" Camera for Precise Mapping and Targeting

Image data can readily be processed to extract coordinates of features.

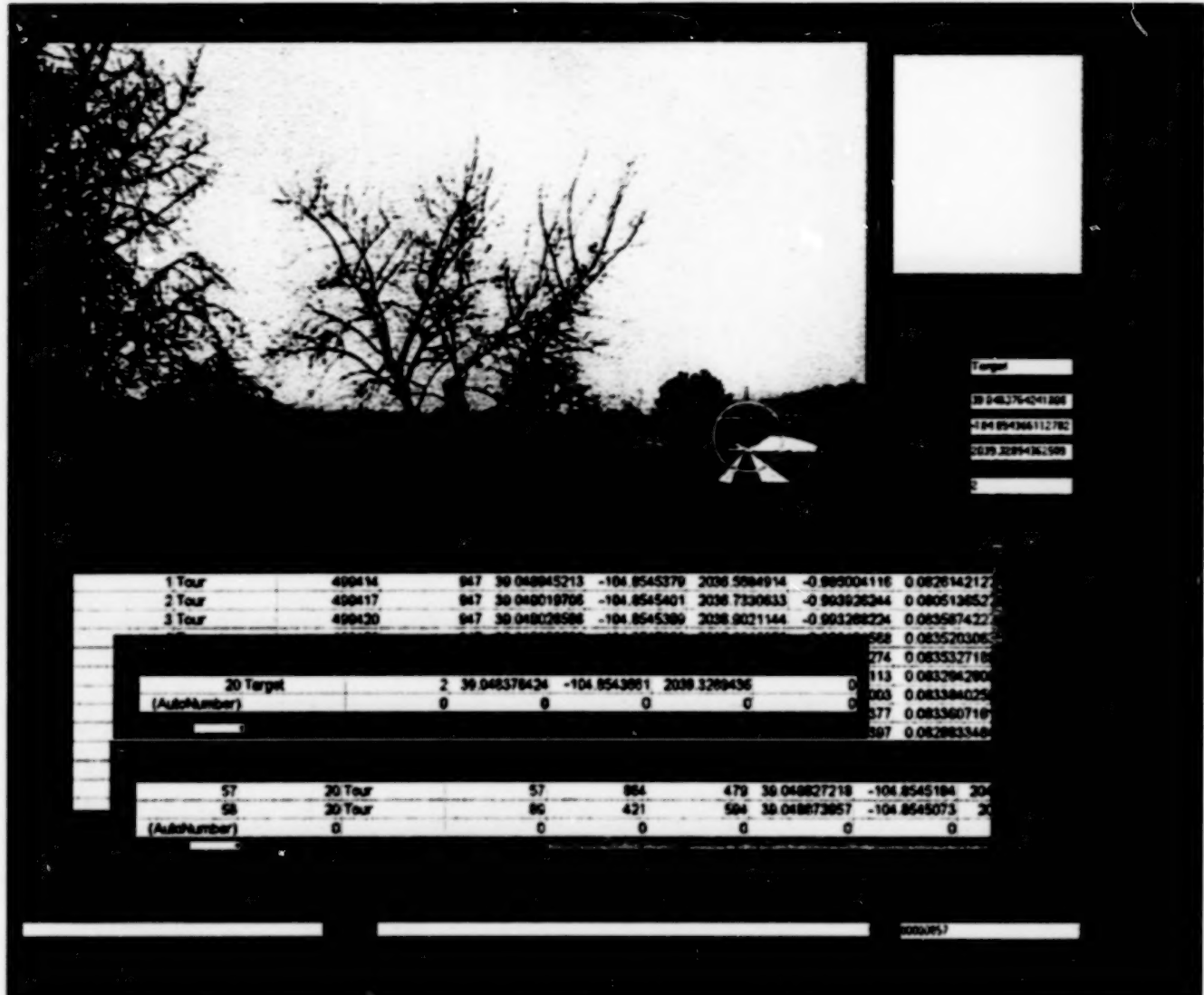
A "smart" video camera, called the "GI-Eye," generates digital image data that are automatically tagged with georegistration meta-data to indicate the precise position and attitude of the camera when the image was taken. This automatic georegistration streamlines the processing of the digital image data; in particular, it

reduces the time needed to correlate common features in different images and enables the derivation, from the image data, of the precise three-dimensional coordinates of features in images.

The GI-Eye includes a Global Positioning System (GPS) receiver, inertial sensors (an accelerometer and a fiber-optic gyro-

NAVSYS Corporation,
Colorado Springs, Colorado

scope), and a digital video camera. The digital image data are recorded in bit-map file format and can be stored on a compact disk read-only memory (CD-ROM) or other personal-computer-compatible mass-data-storage medium for subsequent retrieval. The georegistration meta-data are saved in an Access data base, where they



An Image Containing a Target is overlaid with target information from an object data base in a typical GI-Eye display.

are cross-referenced to the image bit-map filenames to facilitate the retrieval and processing of the image data.

The GI-View software package is designed to facilitate processing of the GI-Eye digital image data and to generate three-dimensional coordinates of features of interest from the image data base (see figure). This software package runs under Windows on a desktop or laptop personal computer. GI-View provides a point-and-click user interface for selection of features from the digital images. When multiple views of the same feature are selected, GI-View automatically computes the three-dimensional coordinates of that feature. The feature coordinates are saved in an Access data base to facilitate the establishment of interfaces with other Windows

application programs or with Geographic Information System (GIS) software.

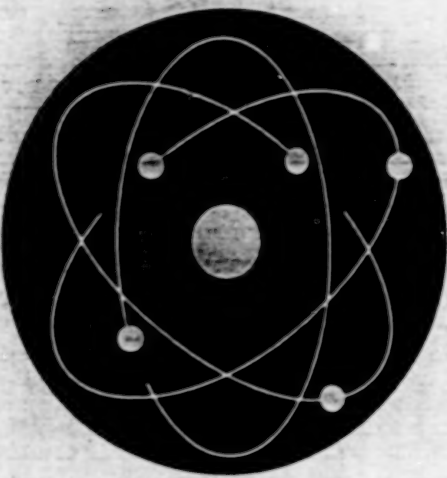
The GI-Eye system has been demonstrated to provide three-dimensional coordinates from the image data to with 1- to 2-meter accuracy at distances of up to 1 km from the camera. For objects that are much closer, the positions of features relative to the location of the camera can be determined to an accuracy of a few centimeters.

The GI-Eye system has been selected by the U.S. Navy for use in an advanced technology demonstration to provide real-time target coordinates on the battlefield. The GI-Eye system is also available for generating GIS attribute databases and providing point coordinates for mapping and surveying.

This work was done by Alison Brown and Randy Silva of NAVSYS Corporation for NASA Headquarters under an SBIR contract to develop a GPS/inertial mapping system and for the Defense Advanced Research Program Agency (DARPA) to develop a precise targeting system. For further information, please contact

Alison Brown
NAVSYS Corporation
14960 Woodcarver Road
Colorado Springs, CO 80921
Tel.: (719) 481-4877
Fax: (719) 481-4908
E-mail: abrown@navsys.com
or access www.navsys.com
Refer to SBIR-0005.

BEST COPY AVAILABLE



Physical Sciences

Hardware, Techniques, and Processes

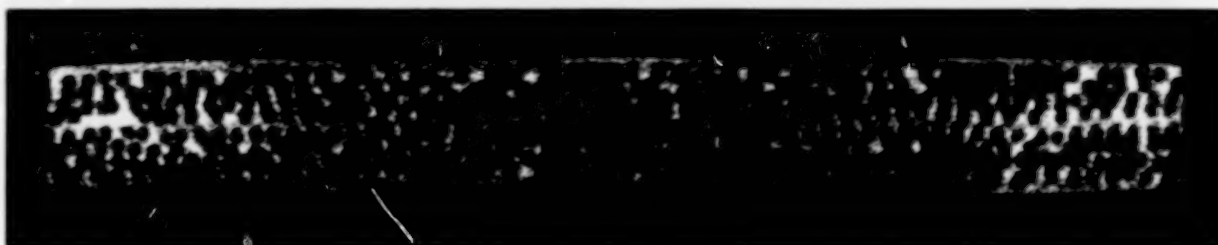
- 23 Using CT Data in Finite-Element Models of MMC Components
- 24 Transparent Furnaces for High-Temperature Research
- 25 Optical Remote Detection of Ice on Aircraft Surfaces
- 26 Remote In-Flight Infrared Imaging for Analyzing Surface Flows
- 26 Measurements of Radiation in the Atmosphere
- 27 Computer-Controlled Instrumentation Measures Hydrogen Leaks

BLANK PAGE

Using CT Data in Finite-Element Models of MMC Components

Computer simulations based on nondestructive computed tomography could replace some costly experiments.

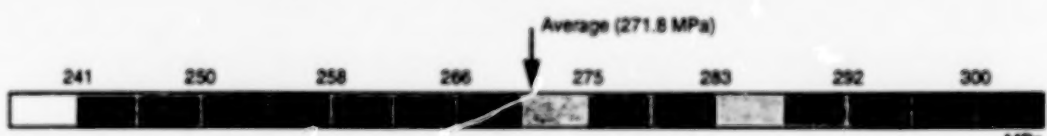
Lewis Research Center,
Cleveland, Ohio



(a) Cross Section of MMC Coupler



(b) Transverse Stress (σ_{xy}) in Response to a Transverse Strain



(c) Von Mises Stress (σ_{VMS}) in Response to a 0.2% Transverse Strain

Figure 1. This Cross Section of an Eight-Ply MMC Coupon was made by CT with sufficient resolution to show individual fibers. Images like these can be digitized, then processed (1) by image-analysis software to obtain fiber volume fractions and (2) by applied load to obtain stress distribution as shown in (b) and (c).

X-ray-based Computed Tomography (CT) has been linked with finite-element analysis to provide a capability for structural characterization of as-manufactured parts — especially for the nondestructive evaluation of metal-matrix composite (MMC) material parts. In some cases, this capability might eventually obviate costly experiments, including destructive experiments that are traditionally performed to determine mechanical responses. Though developed primarily for MMCs, this capability could also be applied to other types of composites, metal forgings and castings, and plastic components.

The basic idea is to utilize data obtained nondestructively to eliminate the need for mechanical testing of a component. In the present approach, one does this by using

a finite-element structural-analysis computer program to predict the behavior of the component under load (including, for example, effects of stress concentrations), in combination with information obtained nondestructively by x-ray CT of the component. In the program, local variations in material properties are approximated by differences among the material-property parameters of the finite elements. The values of the finite-element material parameters are, in turn, calculated from such data as local volume fractions of fibers as determined by analysis of CT imagery.

To link the CT and finite-element-analysis capabilities, it was necessary to develop software to overlay finite-element meshes on CT images, software to manipulate nodes of finite-element meshes to

conform with geometries of tomographic slices, and software to classify and manage input and output data pertaining to each finite element. Two case studies were performed to demonstrate the resulting capability. The first study involved MMC test coupons like that of Figure 1. Image-processing techniques were used to segment the fibers from the matrix, then there was created a finite-element mesh, wherein each finite element had unique stiffness properties based on the volume fraction of fibers in that element as calculated from the segmented CT data. The finite-element analysis showed that concentrations of high-fiber-volume-fraction finite elements produced stress concentrations.

The second case study involved a ring comprising (1) a core made of a com-

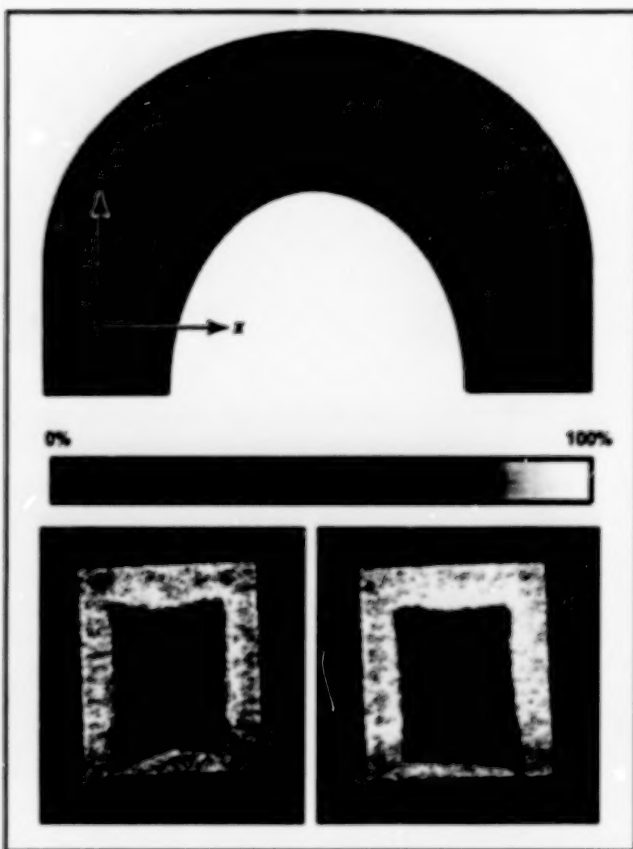


Figure 2. Two Cross-Sectional CT Images of a Composite Ring show imperfections of the Ti-matrix/SiC-fiber core and the Ti cladding.

posite of SiC fibers in a Ti matrix surrounded by (2) Ti cladding and including (3) a damaged area near the outer part of the core. CT cross-sectional images of the ring (see Figure 2) revealed that the core was not uniformly shaped or positioned within the cladding. Several CT cross-sectional images, including the ones in Figure 2, include a bright line across the core that was later determined to represent overlapping of a titanium foil. Variations in the density of the core as shown in the cross-sectional CT images were later correlated with variations in fiber volume fraction. In this study, a finite-element mesh was created to match the ring geometry, and the stiffness parameters in the finite elements in the damaged area were reduced. The results of the finite-element analysis showed that the damaged area could be expected to give rise to stress concentrations elsewhere in the ring.

This work was done by George Y. Baikin of Lewis Research Center and Robert N. Yancey of Advanced Research and Applications Corp. Further information is contained in a TSP [see page 1].

Inquiries concerning rights for the commercial use of this invention should be addressed to NASA Lewis Research Center, Commercial Technology Office, Attn: Tech Brief Patent Status, Mail Stop 7-3, 21000 Brookpark Road, Cleveland, Ohio 44135. Refer to LEW-16618.

Transparent Furnaces for High-Temperature Research

Optical access will contribute to diagnosis and feedback control.

Transparent furnaces are being developed for use in research on properties and processing of materials at high temperatures. Full optical access to the interiors of furnaces is intended to provide the capability for nonintrusive diagnosis and feedback control of the subtleties of high-temperature processes. Small furnace windows are now included in some otherwise opaque furnaces to provide visibility for assessing crystal quality, but only small portions of the objects of interest can be viewed, and these windows cause thermal disturbances that affect crystal-growth processes.

A standard transparent furnace of the type developed thus far includes a quartz tube that is coated with a thin layer of gold and that surrounds the hot zone. The gold layer is about 80 percent transparent to visible light and about 95 percent reflective to infrared radiation; thus, it enables visual observation of the interior of the furnace while acting as a radiant heat insulator to

impede leakage of heat from the furnace.

The furnace is heated by one or more helically wound resistance heating coils. The pitch of the coils is made large enough to make it possible to look between the turns of the coil(s) and see the interior region of interest. A quartz shield tube is located between the heater and the gold-coated mirror surface to prevent the outgassing heater material from coating the gold and thereby reducing its infrared reflectivity. A quartz "muffle" tube is mounted as an impurity barrier between the heater and the material sample to be heated and observed. Typically, the hot zone is 6.5 cm in diameter and 13 cm long, and a controlled atmosphere is maintained in the hot zone.

Standard transparent furnaces developed thus far have been limited to operating temperatures below 1,000 °C. Transparent furnaces at the leading edge of development are being modified for operation at higher temperatures; the

Lewis Research Center, Cleveland, Ohio

modifications include improvements in containment of thermal radiation, reduction in convective transfer of heat, the use of materials that are transparent at high temperatures, and improved design of transparent-heater components. In a theoretical analysis that coupled energy-balance analysis and heat-shield design with modifications of a commercial transparent furnace, it was shown to be feasible to raise the maximum operating temperature to 1,200 °C.

This work was done by David W. Yost of Centon/Vacuum Industries, Inc., for Lewis Research Center. Further information is contained in a TSP [see page 1].

Inquiries concerning rights for the commercial use of this invention should be addressed to NASA Lewis Research Center, Commercial Technology Office, Attn: Tech Brief Patent Status, Mail Stop 7-3, 21000 Brookpark Road, Cleveland, Ohio 44135. Refer to LEW-16064.

Optical Remote Detection of Ice on Aircraft Surfaces

The thickness of ice can be estimated from spectral reflectance.

NASA's Jet Propulsion Laboratory,
Pasadena, California

An imaging spectroscopic technique is undergoing development for use in remote detection of ice and mapping of the thickness of ice on aircraft surfaces. The technique is based on the variation of local spectral reflectance with the depth of ice and/or water on a surface of known aircraft material (typically, aluminum). The spectrum of white light reflected from each surface point includes absorption dips characteristic of any water or and/or ice present at that point, as distinguished from the relatively flat spectral reflectance of aluminum. Thus, the local thickness of ice (and, optionally, water) can be computed from the local spectral reflectance, and the thickness of ice can be mapped by performing this computation for all points in the image.

In experiments to demonstrate the technique, a band-pass liquid-crystal tunable filter (LCTF) and a 16-bit charge-coupled-device (CCD) camera (see Figure 1) were used to image chilled aluminum cells that were, variously, empty or filled with ice or water to various thicknesses. Reference images of a 99-percent-reflectance standard were also acquired. The aluminum, water, ice, and reflectance-standard images were acquired in 21 wavelength bands, each about 10 nm wide, at nominal pass wavelengths from 850 to 1,050 nm. An independent set of data for verification of the spectral images was acquired by use of a point spectrometer.

The spectral image data were corrected for CCD dark current and bias and converted to reflectance units, and regions of interest were chosen for determining the spatially averaged reflectance spectra. Some of the results are plotted in Figure 2, which illustrates how spectra can be used to distinguish between, and estimate thicknesses of, water and ice. The experiments revealed one shortcoming; namely, that specular reflection from the surface of interest can cause saturation in affected CCD pixels. Fortunately, saturated pixels can simply be excluded from processing of image data; this was done during the processing of image data in the experiments.

This work was done by Gregory Bearman, Abhijit Biswas, Thomas Chrien, Robert O. Green, and Peter Green of Caltech for NASA's Jet Propulsion Laboratory. Further information is contained in a TSP [see page 1].
NPO-19929

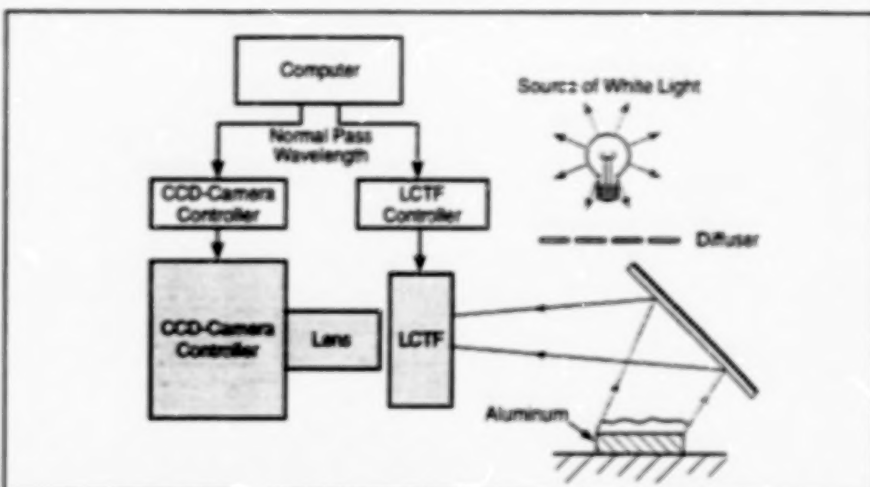


Figure 1. The CCD Camera Looking Through the LCTF acquires images of the same surface in 21 adjacent wavelength bands.

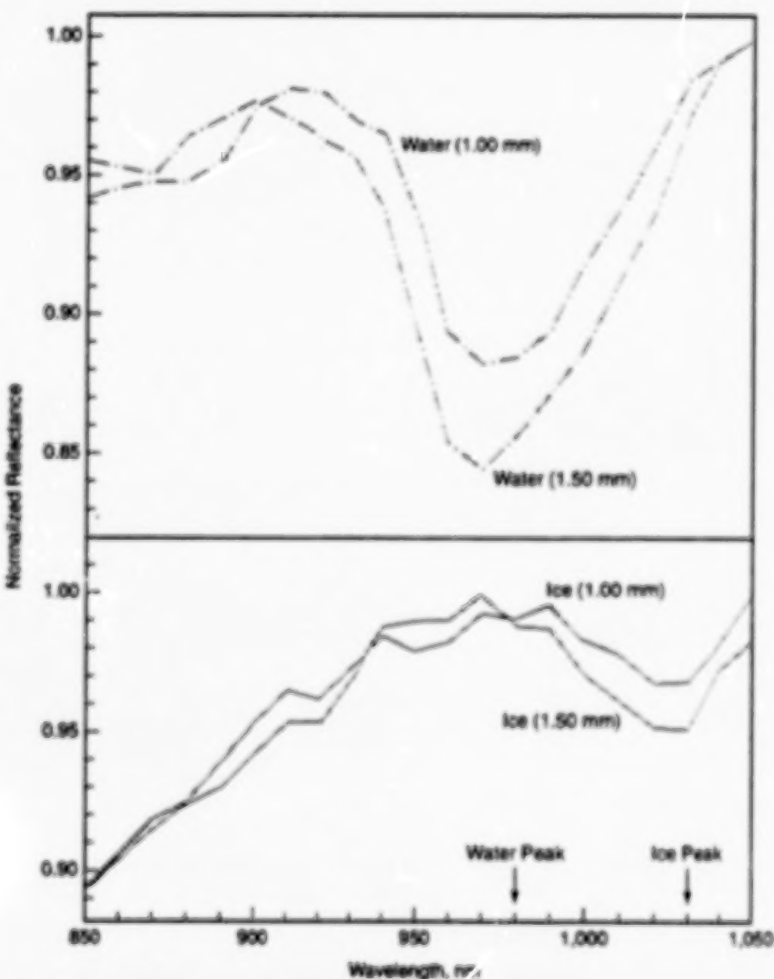


Figure 2. The Spectral Reflectance Ratio is defined here as the spectral reflectance of aluminum covered by water or ice + the spectral reflectance of bare aluminum. The spectral reflectance ratio as a function of wavelength can be analyzed to determine the thickness of ice and/or water. Two depths of ice and water, 1 mm and 1.5 mm, were used.

Remote In-Flight Infrared Imaging for Analyzing Surface Flows

Thermograms reveal some flow features indirectly via effects on surface temperatures.

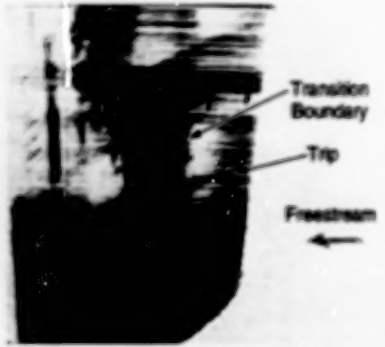
Dryden Flight Research Center,
Edwards, California



F-18 Airplane Equipped To Observe
T-34C Airplane



Outboard Wing of T-34C Airplane in Flight



Transition Pattern on Leading Edge of
Right Wing of T-34C

The Boundary Between Laminar and Turbulent Surface Flows on the wing of a T-34C airplane can be seen in a thermogram acquired by instrumentation aboard an F-18 airplane flying nearby.

The feasibility of remotely acquiring infrared images (thermograms) of aircraft surfaces in flight to locate flow-transition boundaries has been investigated. As used here, "remotely" means that the infrared instrumentation is mounted aboard an observing aircraft that flies along with an observed aircraft, the surface flow on which one seeks to analyze.

Infrared thermograms are, in effect, maps of surface temperatures. Because the rate of mixing in a turbulent boundary layer is greater than in a laminar boundary layer, the turbulent boundary layer transfers heat between the freestream and a surface at a rate greater than that of the laminar boundary layer. Therefore, a surface that is initially warmer than the freestream exhibits a higher temperature in the presence of a laminar than in the presence of a turbulent boundary layer. Similarly, a surface that is cooler than the freestream exhibits a lower temperature in the presence of a laminar than in the presence of a turbulent boundary layer. Therefore, further, one can utilize a thermogram that shows adjacent surface regions with different temperatures to locate the transition between turbulent and laminar boundary layers on the surface.

In-flight thermograms have been acquired from a camera located in or on the aircraft of interest. This approach entailed a number of limitations and disadvantages, including a small field of view and the time and cost of instrumenting each aircraft that one seeks to observe.

In initial tests of the present remote-observation approach, the observing aircraft was an F-18 airplane equipped with a remotely actuated infrared camera and tracking system, and the observed aircraft was a T-34C airplane (see figure). Surface areas of interest were treated by covering them with thin black vinyl contact sheets to minimize reflections, to reduce thermal conductance into the structure, and to raise surface temperature through solar heating.

It was determined from the results of these tests that the desired thermograms can be acquired remotely, and that transition locations and patterns can be extracted from the thermograms. It was also determined that with optimal geometry between the observed and observing aircraft, spatial resolution as low as 0.1 in. (2.5 mm) can be realized. The fields of view obtained in the tests were significantly wider than those in similar images obtained with an on-board system. The images

obtained were comparable in quality to those obtained with an on-board system.

Plans for research to be performed in the near future call for obtaining images from a business jet and a large transport airplane, attempting to depict local shock waves and flow separation in addition to laminar-to-turbulent flow transition, and obtaining images without vinyl surface treatment.

While the remote-observation approach has been found to overcome most of the disadvantages of the previous on-board approach, it entails limitations of its own. These limitations include distortion caused by relative motion between the airplanes during image frames and by changes between observational geometries in successive image frames. Research has been performed to develop a capability to process image data to correct for such distortions and to effect general enhancement of images (e.g., to increase signal-to-noise ratios and optimize contrasts).

This work was done by Daniel W. Banks of Dryden Flight Research Center and C.P. van Dam and Henry J. Shiu of U.C. Davis. Further information is contained in a TSP [see page 1].
DRC-98-73

Measurements of Radiation in the Atmosphere

These measurements are needed to understand changes in climate.

The recent summit meeting held in Kyoto, Japan, has brought world-wide attention to the issue of global climate

change. For the past 5 years, the Department of Energy's Atmospheric Radiation Measurement - Unmanned Aerospace

Dryden Flight Research Center,
Edwards, California

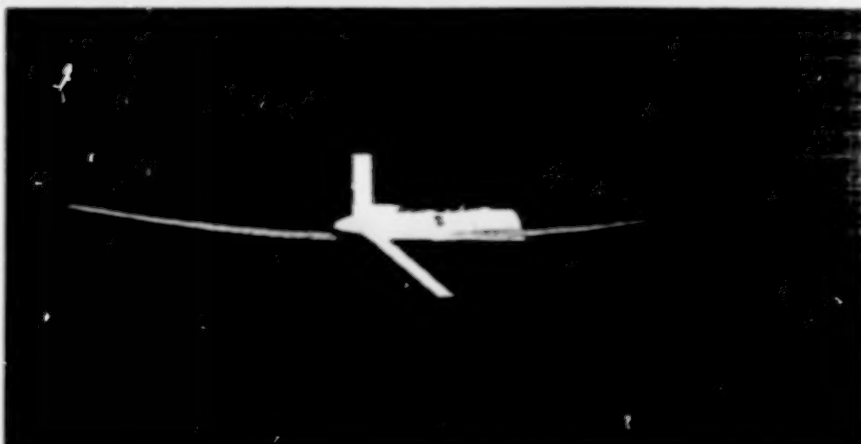
Vehicle (ARM-UAV) Program has been investigating the largest source of uncertainty in global warming: the interaction of

solar radiant energy with clouds. As the program name implies, ARM-UAV is fostering the development of UAVs and developing specialized instruments for measurements related to climate research.

It was recognized from the outset that certain key parameters, such as atmospheric heating and cloud-top properties, are best measured in the atmosphere. The endurance and altitude requirements for these measurements appear to be best met by an emerging class of small, long-endurance, high-altitude UAVs, which complement, but do not eliminate the need for, piloted aircraft, satellites, and surface instrumentation.

In September 1996, ARM-UAV conducted a month-long flight series that culminated in an unprecedented scientific flight extending over a complete day-to-night-to-day cycle (26 hours, 11 minutes). For this flight series, ARM-UAV mounted its payload in the first Altus UAV (see figure), which was built for the NASA Environmental Research Aircraft and Sensor Technology (ERAST) program by General Atomics/Aeronautical Systems, Inc. The ERAST program is managed by Dryden Flight Research Center. This Altus UAV was flown in conjunction with the U.S. Navy's Center for Interdisciplinary Remotely Piloted Aircraft Studies (CIRPAS). ARM-UAV purchased the second Altus UAV for long-term use as an instrumented platform to demonstrate instruments and measurement techniques as well as to acquire initial atmospheric data. The second Altus UAV was first used in a similar month-long flight series in September, 1997, over the DOE's Cloud and Radiation Testbed site in north central Oklahoma.

The primary scientific focus of the ARM-UAV program is on radiation/cloud interactions in atmosphere of the Earth. Uncertainties in how clouds interact with solar and thermal radiation account for almost the entire factor-of-three variation in the predicted temperature rise resulting from a doubling in the carbon dioxide content of the atmosphere. An important aspect of the program is the use of UAVs as the primary airborne instrumentation platforms. UAVs are capable of extended flight at altitudes \geq 65,000 ft (\geq 20 km), making it possible to take continuous



This Altus UAV was photographed in flight over Oklahoma during the ARM-UAV flight series.

measurements with a set of well-calibrated instruments above the tropopause, and thus above the troposphere, which is the lowest layer of the atmosphere where most clouds and weather occur.

The ARM-UAV payload consists of state-of-the-art radiometric instruments, positioned to make measurements above and below the aircraft, and instruments to make such supporting measurements as those of temperature, pressure, and concentration of water vapor. A second, similar payload with the same radiometers is typically flown in a de Havilland Twin Otter airplane, operated by Ross Aviation, flying directly below the Altus UAV. A particularly valuable flight pattern places the Altus UAV above a cloud layer and the Twin Otter below, forming a "cloud sandwich." The simultaneous measurements obtained by the Altus and Twin Otter instruments in this configuration are invaluable in understanding the role of clouds in absorbing and reflecting solar energy.

From the outset, ARM-UAV has been a multiagency program, bringing together the best capabilities available within government agencies, universities, and private industry. Sandia National Laboratories provides overall technical direction, along with logistical planning and support, handling of data, and a multispectral imaging instrument. Other instruments are provided by Goddard Space Flight Center, Ames Research Center, Lawrence Livermore National Laboratory, Brookhaven National Laboratory, and universities, including

Colorado State University and the University of California Scripps Institute. University scientists participating in ARM-UAV are also drawn from the University of Maryland, the University of California at Santa Barbara, Pennsylvania State University, the State University of New York, and others.

The next planned ARM-UAV flight series will be a joint activity with the NASA ERAST program to be conducted in September 1998, from Kauai, Hawaii. The ARM-UAV payload will be installed in the ERAST Altus UAV now being modified to enable flight to altitudes as high as 65,000 ft (20 km). This higher altitude capability will be used to investigate the properties of tropical cirrus clouds.

This article was written by W. R. Bolton of Sandia National Laboratories and describes work done in cooperation with **Dryden Flight Research Center**. Further information is contained in a TSP (see page 1).

In accordance with Public Law 96-517, the contractor has elected to retain title to this invention. Inquiries concerning rights for its commercial use should be addressed to

Sandia National Laboratories

W. R. Bolton

Tel.: (925)294-2203

Fax: (925)294-1377

E-mail: wrbolto@sandia.gov

Refer to DRC-98-32, volume and number of this NASA Tech Briefs issue, and the page number.

Computer-Controlled Instrumentation Measures Hydrogen Leaks

An instrumentation system monitors rates of leakage of hydrogen from multiple zones on a complexly shaped tank. Each zone is established by bagging a

designated exterior portion of the tank. The bag for each zone is purged with a carrier gas (either nitrogen or helium) at a controlled flow rate, then the carrier gas

with leaked hydrogen (if any) mixed in is routed to one of two mass spectrometers, which can measure concentrations of hydrogen from 30 parts per million to 4

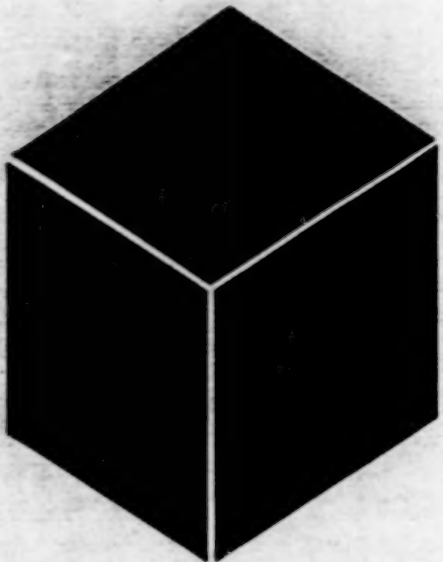
percent calibrated. Microelectronic sensors are used to measure concentrations from 2.5 to 100 percent, enabling the hydrogen concentration to be determined after the mass spectrometers have reached their saturation point. Inlet valves on each mass spectrometer enable the selection of purge exhaust to be sampled from any of eight zones. The microelectronic sensors are positioned in

the exhaust flow from the mass spectrometers. A computer, acting via a programmable-logic controller, monitors and controls valves, flow-control valves, and related instrumentation. Another computer monitors and controls the mass spectrometers. Hydrogen-concentration data acquired by the mass-spectrometer-control computer are fed to the flow-control computer, which computes hydrogen-

leak rates from the measured hydrogen concentrations and flow rates. The microelectronic-sensor data are recorded by the facility Data Acquisition System.

This work was done by Glenn Varner of Stennis Space Center and Phillip Hebert and Lester Langford of Lockheed Martin. Further information is contained in a TSP [see page 1].

SSC-00065



Materials

Hardware, Techniques, and Processes

31	MoSi ₂ -Based Composite Materials for Aircraft Engines
32	Metal- and Oxide-Containing Carbons Made From Graphite Oxide

BLANK PAGE

MoSi₂-Based Composite Materials for Aircraft Engines

These lightweight materials may eventually supplant nickel-based superalloys in some components.

Lewis Research Center,
Cleveland, Ohio

MoSi₂-based composite materials are among the advanced materials undergoing development as potential strong, stiff, lightweight replacements for the nickel-based superalloys now used in aircraft engines. Of the MoSi₂-based composites, the most promising ones include SiC-based fibers within matrices that are, themselves, composites of MoSi₂ containing 30 to 50 volume percent of Si₃N₄ particles.

MoSi₂ exhibits suitable high-temperature oxidation behavior, along with lower density and higher melting temperature relative to superalloys. However, the use of MoSi₂ has been hindered by brittleness at low temperatures, inadequate resistance to creep at high temperatures, a coefficient of thermal expansion (CTE) much greater than that of SiC and other candidate fiber reinforcement materials, and a phenomenon called "pesting" (described in the next paragraph) at temperatures in the approximate range of 400 to 500 °C.

Pesting, also called "pest oxidation," is usually defined as disintegration into powder. Pesting is considered to result from accelerated oxidation, among other things. In the case of MoSi₂, pesting involves the simultaneous formation of MoO₃ and SiO₂. In most cases, pesting in MoSi₂ has been linked to the formation of voluminous Mo oxides in pores or microcracks.

Since 1985, considerable research effort has been directed toward improving the high-temperature performance of MoSi₂ by solid-solution alloying, reinforcement by fibers, and reinforcement by discontinuous inclusions. The present line of development of (MoSi₂/Si₃N₄)-matrix/SiC-fiber composites is a logical sequel to previous research that yielded the following findings pertaining to the MoSi₂/Si₃N₄ material system:

- The addition of 30 to 50 volume percent of Si₃N₄ particles to MoSi₂ increased resistance to low-temperature accelerated oxidation through the formation of a Si₂ON₂ protective scale, thereby eliminating catastrophic pest failure.
- The addition of Si₃N₄ particles also increased compressive strength, fracture toughness, and high-temperature oxidation resistance.
- The brittle-to-ductile transition temperature of MoSi₂ containing 30 volume percent of Si₃N₄ particles was found to lie between 900 and 1,000 °C.



This Scanning Electron Micrograph depicts a cross section of a composite of (1) MoSi₂ matrix containing 30 volume percent of Si₃N₄ particles and (2) commercial SiC-based fibers.

- The CTE of MoSi₂ containing Si₃N₄ particles was significantly less than that of pure MoSi₂. As a result, unlike the matrices in MoSi₂-matrix/SiC-fiber composites, the matrices in (MoSi₂/Si₃N₄)-matrix/SiC-fiber composites did not exhibit cracking, even after thermal cycling.

To fabricate specimens for experiments along the present line of development, mixtures of MoSi₂ and Si₃N₄ powders were prepared, then consolidated by hot vacuum pressing followed by hot isostatic pressing to form fully dense plates of matrix-only (MoSi₂/Si₃N₄) material. Specimens of (MoSi₂/Si₃N₄)-matrix/SiC-fiber composites (see figure) were prepared similarly, except that multiple plies of SiC-based fibers in various orientations were interspersed with the mixed MoSi₂ and Si₃N₄ powders before pressing. (More recently, tape casting was adopted as the preferred technique for processing the fiber and matrix materials with improved fiber spacing, the ability to use narrower fibers, and lower cost.) The two-step consolidation procedure enabled the use of a consolidation temperature lower than that needed if consolidation were effected by hot pressing alone. The use of the two-step, lower-temperature consolidation procedure resulted in a fully dense material without excessive chemical reactions or damage to the fibers.

The specimens were subjected to a variety of tests to characterize their mechanical, thermal, microstructural, and chemical properties at temperatures ranging up to about 1,400 °C. The results of the experiments agreed with the previous findings and led to the following (among other) additional findings:

- The addition of Si₃N₄ to MoSi₂ doubled the room-temperature toughness and reduced the high-temperature creep rate by about 5 orders of magnitude.
- Reinforcement of MoSi₂/Si₃N₄ matrix materials by SiC-based fibers increased room-temperature fracture toughnesses by factors of about 7 and impact resistance by factors of about 5.
- In general, specimens of (MoSi₂/Si₃N₄)-matrix/SiC-fiber composites exhibited excellent strength and toughness improvements at temperatures up to 1,400 °C.

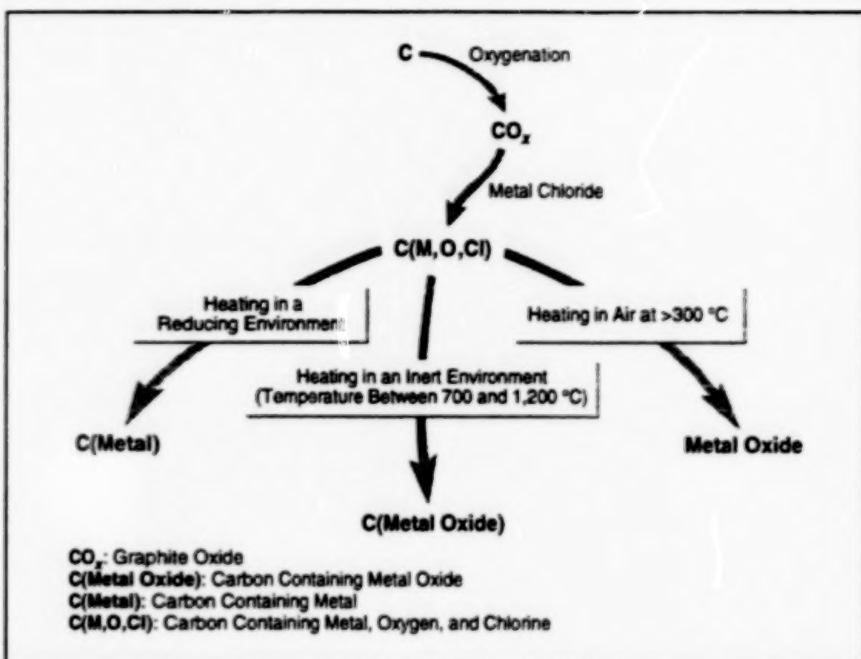
This work was done by M. V. Nathal of Lewis Research Center and M. G. Hebsur of NYMA, Inc. Further information is contained in a TSP [see page 1].

Inquiries concerning rights for the commercial use of this invention should be addressed to NASA Lewis Research Center, Commercial Technology Office, Attn: Tech Brief Patent Status, Mail Stop 7-3, 21000 Brookpark Road, Cleveland, Ohio 44135. Refer to LEW-16617.

Metal- and Oxide-Containing Carbons Made From Graphite Oxide

These materials can be used in gas sensors, power cells, and catalytic cells.

Lewis Research Center,
Cleveland, Ohio



A Carbon Material Is Partly Oxidized to obtain graphite oxide, which is treated with a metal chloride, then heated in a reducing, oxidizing, or inert environment to obtain one of three types of end products.

Carbon-based materials containing, variously, metals and metal oxides can be synthesized according to a method that involves reactions of metal chlorides with materials of general composition CO_x . In a typical material synthesized by the present method, the carbon is porous and serves as a substrate for the metal or metal oxide. Depending on the application, the metal or metal oxide could serve, for example, as a catalyst or as an electrode material in a gas sensor or electrochemical power cell. Alternatively, instead of serving as a substrate, the carbon could serve as a template for formation of a porous metal oxide (ceramic), from which the carbon is eventually removed.

Aspects of a related older method were described in several previous articles in *NASA Tech Briefs*, including "Iron-Containing Carbon Materials Made From Graphite Fluoride" (LEW-16432) Vol. 22, No. 5 (May 1998), page 46 and "Modifi-

cation of Carbon Fibers for Higher Young's Modulus" (LEW-15847) *NASA Tech Briefs*, Vol. 21, No. 4 (April 1997), page 56. The corrosiveness and toxicity of fluorine and the general difficulty and high cost of synthesizing graphite fluoride make the older method unattractive. Among the advantages of the present method are that in comparison with graphite fluoride, graphite oxide is safer and can be made more easily (under lower temperatures and otherwise milder conditions) and at lower cost.

Denoted loosely as graphite oxide (or sometimes as graphitic oxide or graphite acid), CO_x is a yellow-brown material that was first synthesized in 1859. In most of the known procedures for synthesizing CO_x , graphite is treated with oxidizing mixtures that contain concentrated acids and oxidizing materials. One such procedure, published in 1958, involves the treatment of graphite with an initially water-free mixture of concentrated sulfuric acid, sodium

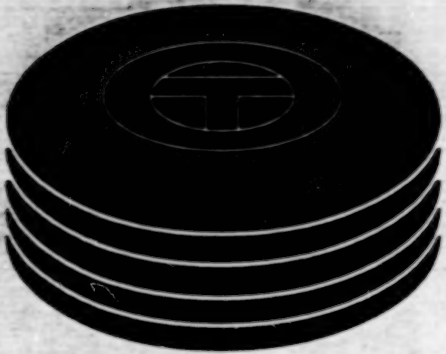
nitrate, and potassium permanganate. This procedure was used to prepare CO_x for use in initial experiments to demonstrate the present method of synthesizing carbon-based materials containing metals and oxides.

The figure illustrates a generic process for making a carbon-based material containing a metal or metal oxide according to the present method. The starting carbon material can be crystalline graphite, amorphous carbon, or graphitized carbon in fiber or powder form. The carbon material is treated as described above to obtain CO_x , which is then exposed to a metal chloride at a temperature between ambient and 200 °C. The metal chloride can be in the form of a solution, a pure liquid, a pure vapor, or a mixture of two or more of these forms. The resulting intermediate product, denoted " $\text{C}(\text{M}, \text{O}, \text{Cl})$," consists of carbon filled with the metal, chlorine, and oxygen in various proportions.

Heating the $\text{C}(\text{M}, \text{O}, \text{Cl})$ in air at a temperature $>300^\circ\text{C}$ causes oxidation and consequent removal of the carbon and chlorine, yielding a porous metal oxide. Heating the $\text{C}(\text{M}, \text{O}, \text{Cl})$ in a reducing environment yields porous carbon containing metal particles. Heating the $\text{C}(\text{M}, \text{O}, \text{Cl})$ in an inert atmosphere (e.g., N_2 or Ar) at a temperature between 700 and 1,200 °C removes some or all of the chlorine, yielding a porous carbon containing a metal oxide.

This work was done by Ching-cheh Hung of Lewis Research Center. Further information is contained in a TSP [see page 1].

Inquiries concerning rights for the commercial use of this invention should be addressed to NASA Lewis Research Center, Commercial Technology Office, Attn: Tech Brief Patent Status, Mail Stop 7-3, 21000 Brookpark Road, Cleveland, Ohio 44135. Refer to LEW-16342.



Computer Programs

Mathematics and Information Sciences

35 Simulation by Logical Modeling of Costs

BLANK PAGE

Computer Programs

These programs may be obtained from COSMIC. Please contact

COSMIC®

Computer Services Annex
University of Georgia
Athens, GA 30602
Telephone No. (404) 542-3265.

Mathematics and Information Sciences

Simulation by Logical Modeling of Costs

Labor hours and costs in a specific application can be projected for multiple years.

The Simulation by Logical Modeling of Costs (SIBYL/COST) software subsystem is used by logistical and financial analysts to develop cost projections of labor and hardware requirements for preparation of space shuttle main engine

(SSME) spares proposals, SSME program operating plans (POPs), and special engine-cost studies. SIBYL/COST makes projections of program resource requirements, identifies potential program threats and associated costs, evaluates adjustments of scope to meet funding levels, supports decision packages for pre- and post-POP exercises, and provides sufficient detail to support operating plans, team budgets, and changes in contracts for subsequent years.

Pricing, financial, and logistical analysts and team members use SIBYL/COST to make multiyear labor-hour and cost projections. The analyst starts the program by opening a new data file, which provides default component names, configurations, hardware schedule, and such tables as those of accounting hours and ogives. The team members then enter discrete data based on hardware schedule provided by the financial analyst. As each team's data become available, the financial analyst imports the team's discrete data into a central data file. Upon completion of this process, the financial analyst generates a multiyear projection

of labor hours and costs.

SIBYL/COST is written in C++ for use on IBM-compatible personal computers running the Windows 3.1 operating system. It has been successfully implemented under Windows 3.1, Windows 95, and Windows NT 4.0. An executable program, together with sample input and output data files, is included. Btrieve for Windows and Spread/VBX are necessary if there is a need to recompile source code. To obtain a copy of Btrieve, call Pervasive Software at 1-800-287-4383. To obtain Spread/VBX, call FarPoint Technologies, Inc., at 1-800-645-5913. The standard distribution medium for SIBYL/COST is a set of three 3.5-in. (8.89-cm), 1.44MB diskettes in MD-DOS format. The contents of diskettes 2 and 3 have been compressed by use of the PKWARE archiving software tools. SIBYL/COST was released to COSMIC in 1997.

This program was written by John K. Fredrick, William R. Jennings, and Hyon Ok Wu of Boeing North American for Marshall Space Flight Center. Further information is contained in a TSP [see page 1].
MFS-30139

BLANK PAGE



Mechanics

Hardware, Techniques, and Processes

- 39 Flush Airdata Sensing System for the X-33 Aerospace Vehicle
- 40 Electrostatic Displacement Control Compensates for Spring
- 41 Program Facilitates Simulation of Flows of Cryogenic Fluids

BLANK PAGE

Flush Airdata Sensing System for the X-33 Aerospace Vehicle

Features include dual redundancy and an improved algorithm for processing measurements.

Dryden Flight Research Center,
Edwards, California

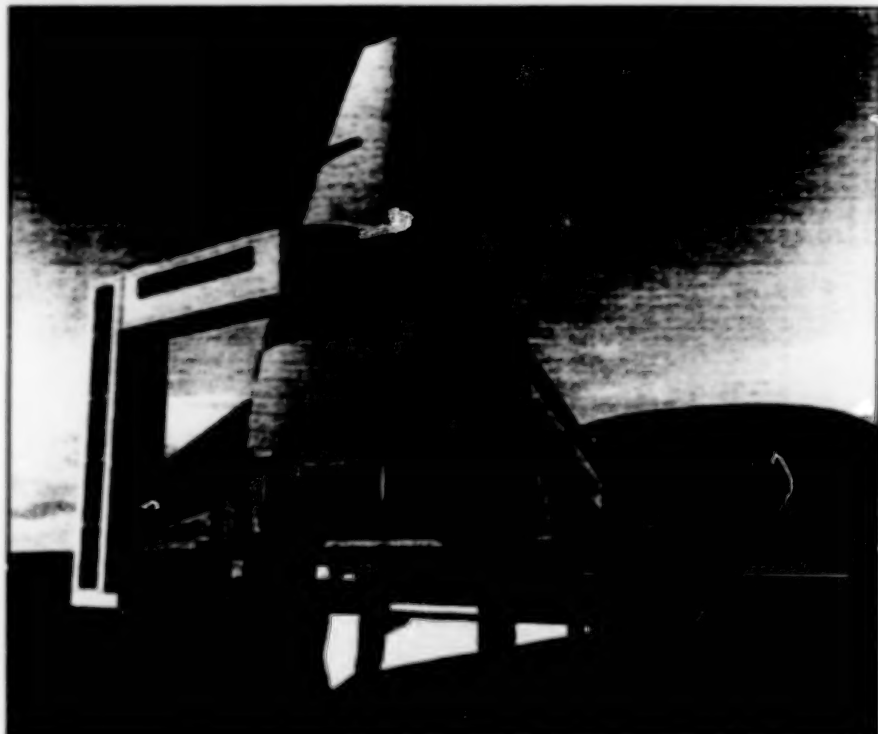
A novel airdata system based on flush-mounted pressure sensors has been developed for the X-33 aerospace vehicle. Denoted the "X-33 flush airdata sensing" (FADS) system, it was designed to overcome limitations of pitot-static probes that were used previously, as explained below.

The X-33 is an autonomous, lifting-body-type demonstrator aerospace vehicle designed for use in validating those items of technology necessary for development of single-stage-to-orbit launch vehicle. The sensors in the original X-33 airdata system were a pair of pitot-static probes (like those used on the Space Shuttle Orbiter) that were deployed on a roll-over mechanism after completion of the high-heat atmospheric-reentry phase of flight. These probes were undesirable for several reasons, including difficulty of integration into the X-33 structure, lack of way to achieve accurate calibration for the first few flights, and lack of a method for measuring sideslip.

The foregoing considerations, along with the success of several recent FADS-system flight-test programs at NASA Dryden Flight Research Center, led to the decision to use a FADS on the X-33 vehicle. The X-33 FADS system was required to provide valid airdata below mach 4 during the launch and landing phases of flight, and to remain operational with a single failure anywhere in the system.

An airdata sensing system is needed because the X-33 flight-control and guidance software require the airdata state of the vehicle during the launch, terminal-area energy-management (TAEM), approach, and landing portions of the flight trajectory. Inertial systems are not acceptable because they do not account for wind conditions. Minimizing the angle of attack and amount of sideslip of the X-33 vehicle during the launch portion reduces the loads on the airframe. During the TAEM, approach, and landing portions, the mach number, velocity, and angle of sideslip are used to improve flying qualities and compensate for the wind conditions.

The hardware of the X-33 FADS system measures pressures at six locations on the nose cap of the vehicle. At each location, there are two ports, which are plumbed to individual absolute-pressure



The X-33 Aerospace Vehicle will be launched vertically like a rocket and will land horizontally like an airplane. It will reach altitudes as high as 50 mi (80 km) and speeds as high as mach 15. It will not carry a crew or cargo; it will be used for testing and demonstration only.

transducers to create a dual redundant system with no moving parts. The FADS algorithm, which was developed by Dryden Flight Research Center, includes a calibrateable pressure-distribution mathematical model, through which the measured pressures are related to the vehicle airdata. This model is a splice of (1) the closed-form potential-flow solution for a blunt body, applicable at low subsonic speeds; and (2) the modified Newtonian flow model, applicable at hypersonic speeds. Data from wind-tunnel tests have been used to calibrate the X-33 FADS model for the effects of flow compression, body shape, and such other systematic effects as shock-wave compression or Prandtl-Meyer expansion on the forebody. Once calibrated, the model can be inverted in real time to calculate the airdata state, to the required accuracy, as a function of the measured pressures.

Some innovations have been made to improve upon the previous FADS design for the X-33 application:

- An improved solution subalgorithm for the FADS pressure model makes it pos-

sible to decouple (1) the computation of flow-incidence angle, angle of attack, and sideslip from (2) the solution for the mach number, static pressure, and total pressure. This decoupling offers several software and redundancy-management benefits.

- A measure of the error in the pressure-model is used to select the better of the dual-redundant airdata subsystems. This feature makes it possible for both soft and hard failures, including undetected failures, to occur in one subsystem without degrading the airdata computation. This level of redundancy, referred to as "fail-operational," typically requires a mid-value selection of a triple-redundant system.
- A methodology for analyzing the stability of the FADS algorithm was also developed.

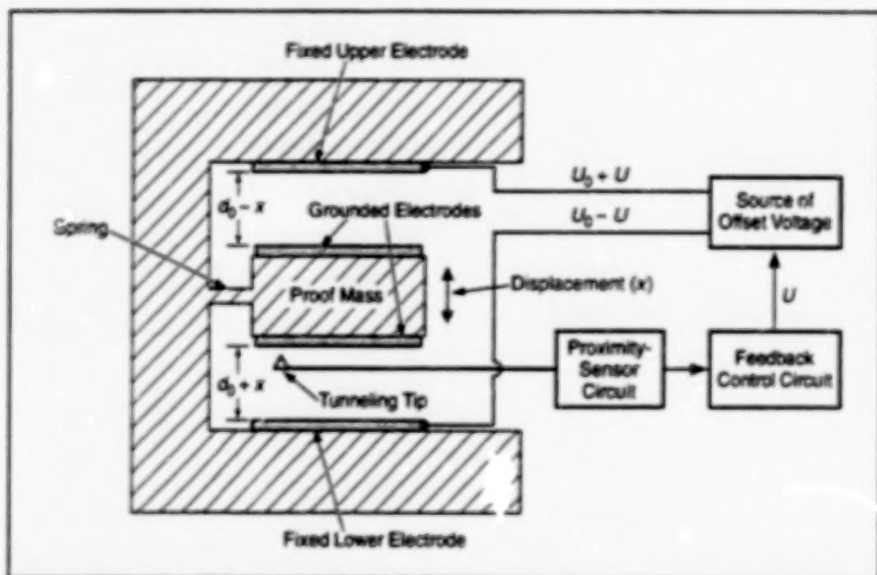
This work was done by Stephen A. Whitmore, Brent Cobleigh, and Ed Haering, Jr., of Dryden Flight Research Center. Further information is contained in a TSP [see page 1].

DRC-98-55

Electrostatic Displacement Control Compensates for Spring

Effective spring stiffness is reduced to near zero, greatly increasing low-frequency response.

NASA's Jet Propulsion Laboratory,
Pasadena, California



This Accelerometer Is Similar to previously reported micromachined spring-and-mass accelerometers with feedback electrostatic displacement control, except that the offset voltage U_0 can be chosen to compensate for the spring stiffness, yielding nearly zero effective spring stiffness and correspondingly increased low-frequency response.

The figure schematically illustrates part of an accelerometer in which a feedback control subsystem applies voltages to generate electrostatic forces to minimize the displacement of a proof mass suspended on a spring. Older systems of this type provide active control of the displacements of proof masses but do not provide any compensation for spring stiffnesses; as a result, low-frequency responses are characterized by displacement errors proportional to mechanical resonance frequencies. The present system differs from older systems in that it operates with a combination of voltages chosen to produce not only active control of the displacement of the proof mass but also passive compensation for the stiffness of the spring. Consequently, in the present system, the effective spring stiffness and resonance frequency are reduced to near zero, and the low-frequency position error is greatly reduced.

The proximity-sensor circuit measures the displacement of the proof mass relative to a nominal position along a direction between the fixed electrodes. The prox-

imity sensor in this system is a quantum-mechanical-tunneling tip, but a capacitor electrode or other suitable device could also be used. The output of the proximity-sensor circuit is processed through feedback control electronic circuitry, which generates electrostatic deflection voltages to drive the displacement toward zero. One of the electrostatic deflection voltages is taken as a measure of the force tending to displace the proof mass, and thus as a measure of acceleration.

The electrodes on the proof mass are grounded. The voltages applied to the upper and lower fixed electrodes are $U_0 + U$ and $U_0 - U$, respectively, where U is the output voltage generated by the feedback control subsystem and U_0 is a fixed offset voltage that can be chosen to compensate for the spring stiffness. More specifically, one can choose U_0 so that the net component of electrostatic force associated with U_0 and favoring a small displacement is equal in magnitude to the spring force that opposes the displacement.

One can calculate the required value of

U_0 with the help of some simplifying assumptions that include linearity of the spring response; coincidence of the nominal, equilibrium, and middle positions; smallness of displacement relative to the equilibrium electrode separation d_0 ; absence of irreversible processes; absence of slow drifts in mechanical and electronic responses; absence of parasitic feedback loops associated with stray capacitances; and attribution of all errors to noise sources only. In the special case in which the accelerometer is oriented with its sensory (displacement) vertical in a gravitational field and $U = U_0$ is needed to keep the proof mass at the nominal position, the value of U_0 needed to compensate for the spring stiffness is given by

$$U_0 = U_0 d_0 \omega_0^2 / g,$$

where ω_0 is the resonance frequency and g is the gravitational acceleration.

In tests, the accelerometer was used to measure small vertical accelerations. Although designed for use aboard a spacecraft, the accelerometer also performed well in normal Earth gravitation: it was demonstrated to respond to accelerations as small as 10^{-6} g, at frequencies from 0.01 to 20 Hz.

This work was done by Benjamin Dolgin, Boris Lurie, and Paul Zavacky of Caltech for NASA's Jet Propulsion Laboratory. Further information is contained in a TSP [see page 1].

In accordance with Public Law 96-517, the contractor has elected to retain title to this invention. Inquiries concerning rights for its commercial use should be addressed to

Technology Reporting Office
JPL
Mail Stop 122-116
4800 Oak Grove Drive
Pasadena, CA 91109
(818) 354-2240

Refer to NPO-20292, volume and number of this NASA Tech Briefs issue, and the page number.

Program Facilitates Simulation of Flows of Cryogenic Fluids

Expertise in numerical simulation is not needed for routine use.

EASY/ROCETS is a developmental computer program for mathematical modeling and analysis of dynamic flows of cryogenic fluids in a rocket-engine-testing facility. Heretofore, the numerical simulation of such flows has been accomplished by use of computer codes specific to test-equipment configurations. The complexity of these codes has made it necessary to employ numerical-simulation experts to modify the software for each new configuration. In contrast, EASY/ROCETS is a modular software package that can readily be modified, by choice of modules, for different configurations. Thus, EASY/ROCETS enables engineers who lack advanced numerical-simulation expertise to construct useful mathematical models of test systems, leading to better testing of rocket engines. In so doing, this software also relieves numerical-simulation experts of the burden of day-to-day involvement in modifications of test equipment, enabling them to devote more effort to development of improved component mathematical models that can then be incorporated into the software.

EASY/ROCETS has been constructed from the EASY5x and Rocket Engine Transient Simulator (ROCETS) programs. EASY5x is a commercial software package that provides a graphical user interface to expedite the layout and modification of a

system, plotting capabilities that can be utilized for quick display of data, and a numerical-integration engine with several options for analysis. EASY5x also provides representations of basic control system components, which can be used for modeling test-facility control systems.

ROCETS, developed previously under a contract for NACA, is a modular program that provides mathematical-modeling and numerical-simulation capabilities for analysis of flows in rocket engines. A major underlying assumption of ROCETS, and thus of EASY/ROCETS, is that dynamic flows of cryogenic fluids can be approximated satisfactorily by use of lumped-parameter component models. This assumption is valid in most situations encountered in ground testing of rocket engines.

ROCETS includes modules for calculating pressures, mass flow rates, and heat fluxes for flows of compressible and incompressible fluids in pipes, valves, tanks, and heat exchangers. It also includes modules representing turbomachines, properties of constituent fluids (H_2 , O_2 , He, and N_2), and combustion of H_2 and O_2 .

Prior to the development of EASY/ROCETS, ROCETS in its original form was complex enough that a numerical-simulation expert was needed during use to

Stennis Space Center,
Mississippi

ensure proper connections among modules. Fortunately, ROCETS fits well within the EASY5x software environment. The aforementioned modules have been converted, and new engineering modules are undergoing development.

A license from Boeing Computer Services is required for the use of the EASY5x component of EASY/ROCETS. The user needs either a UNIX computer workstation or a Microsoft Windows NT computer to run EASY/ROCETS. A FORTRAN 77 compiler and a PostScript printer are also required, regardless of the computer system.

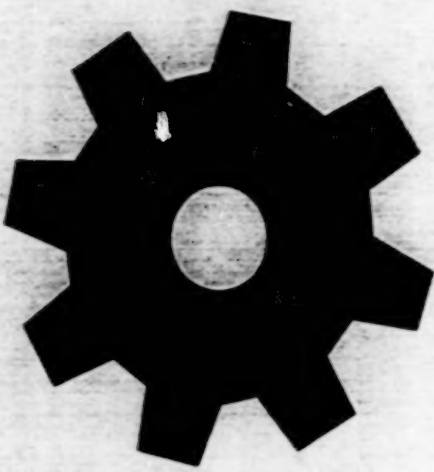
This work was done by Randolph F. Follett and Robert P. Taylor of Mississippi State University for Stennis Space Center.

In accordance with Public Law 96-517, the contractor has elected to retain title to this invention. Inquiries concerning rights for its commercial use should be addressed to

Robert L. Palmer
Mississippi State University
PO Box 6156
Mississippi State, MS 39762-5368
(601)325-3521

Refer to SSC-00044, volume and number of this NASA Tech Briefs issue, and the page number.

BLANK PAGE



Machinery

Hardware, Techniques, and Processes

- 45 Rib Valve as Shutter for Air Swirler in Combustor Nozzle
- 46 Methodology for Optimizing Designs of Rotating Turbine Disks
- 46 Biomimetic Explorers
- 47 Walking Robot for Internal Inspection of Thin-Wall Ducts
- 48 Improved Roller and Gear Drives for Robots and Vehicles

BLANK PAGE

Rib Valve as Shutter for Air Swirler in Combustor Nozzle

Airflow can be adjusted to suit the variable configuration of the combustor.

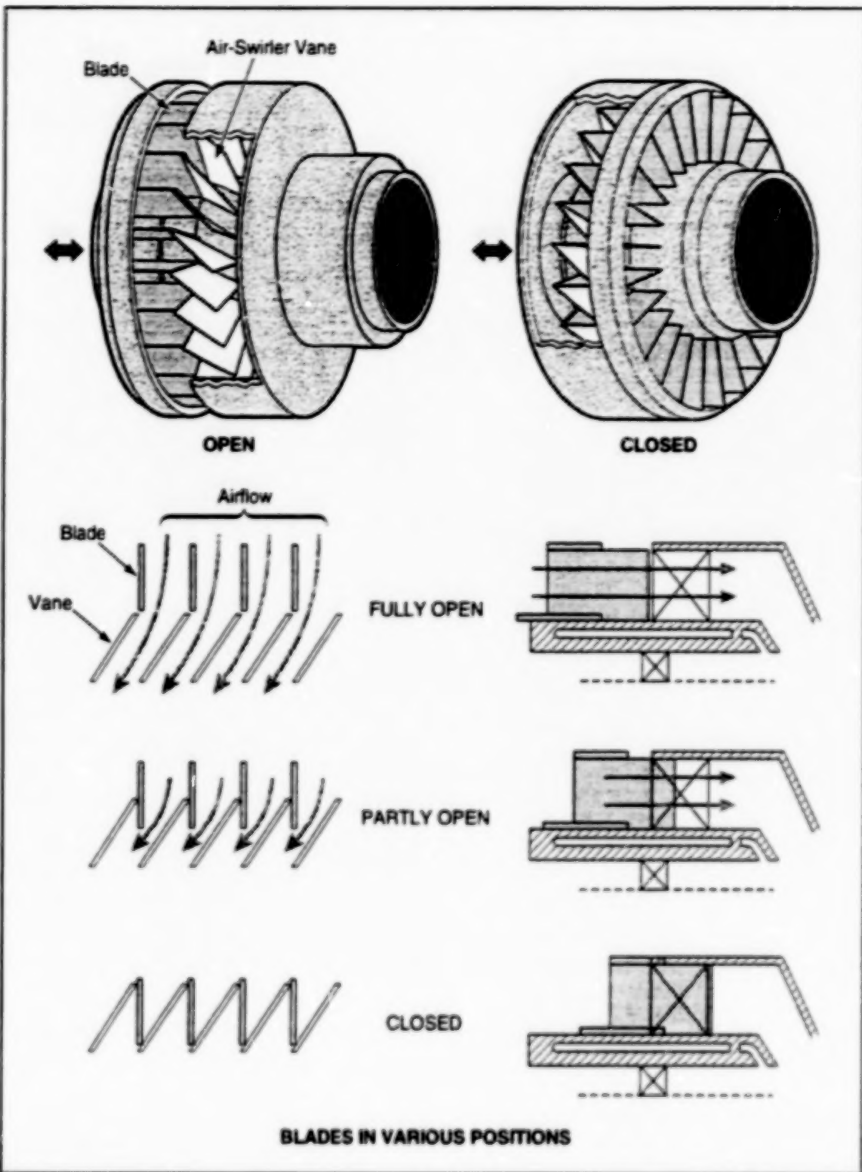
Lewis Research Center,
Cleveland, Ohio

A rib valve is under consideration for use as a shutter in an air swirler in the fuel nozzle of a variable-geometry combustor. In the original application, the variable-geometry combustor would be part of an engine in the High-Speed Civil Transport. In this application, the rib valve/shutter would provide the variable-geometry airflow needed for proper functioning of the combustor under various operating conditions, including rich burn, quick quench, and lean burn. In this context, "proper functioning" means not only smooth and efficient operation but also minimization of quantities of harmful exhaust gases. The rib-valve and variable-geometry combustor design might also be adaptable to any future gas turbine engines.

The rib valve is built into the air swirler (see figure). The air-swirler vanes are mounted in a stationary subassembly. The ribs are straight blades that are located between the air-swirler vanes and are mounted in another subassembly that can be moved axially to insert the blades between the vanes or withdraw the blades from between the vanes. When the blades are fully withdrawn, the air flows axially into the swirler, with very little obstruction — almost as though the blades were not present. When the blades are inserted all the way, the passages between the vanes are blocked, shutting off the flow of swirling air. Flow conditions between these extremes are obtained by moving the blades to intermediate positions.

The rib valve offers advantages over a block valve that is similar except that (a) throttling is effected by an annular disk, the axial position of which can be adjusted to obtain various degrees of partial blockage of the inlet to the air-swirler-vane subassembly and (b) as a consequence, air enters radially, then turns to flow axially. The effective opening area of the block valve in the fully open position is about 10 percent less than that of the rib valve in the fully open position; as a result, the pressure loss in the block valve is almost 20 percent more than that in the rib valve.

One of the consequences of the rib-



Ganged Blades are moved axially between the air-swirler vanes to obtain the required degree of partial blockage of airflow.

valve design is that the velocity of the airflow is nearly uniformly high across the radial flow gap. This is an advantage in that high velocity is needed for adequate atomization of fuel near a fuel filer in the nozzle. In the block valve, the velocity is low near the fuel filer, and the flow profile is skewed when the valve is half open.

This work was done by Qiang Wang of United Technologies for Lewis

Research Center. Further information is contained in a TSP [see page 1].

Inquiries concerning rights for the commercial use of this invention should be addressed to NASA Lewis Research Center, Commercial Technology Office, Attn: Tech Brief Patent Status, Mail Stop 7-3, 21000 Brookpark Road, Cleveland, Ohio 44135. Refer to LEW-16033.

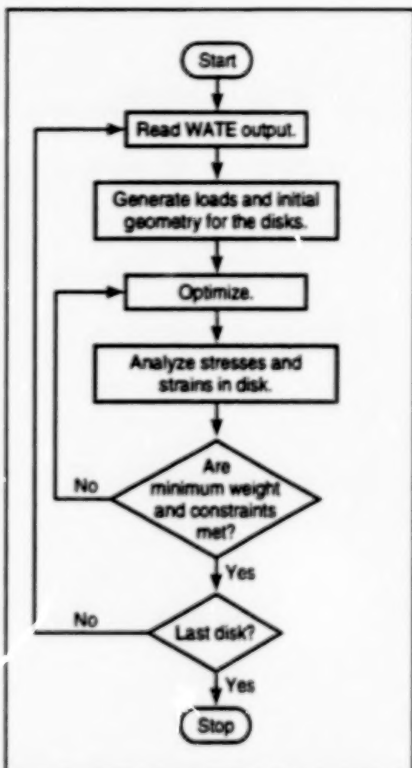
Methodology for Optimizing Designs of Rotating Turbine Disks

Optimization time can be shortened from as much as three weeks to no more than five minutes.

A methodology for optimizing the fundamental structural designs of rotating turbine disks has been developed to aid in preliminary evaluations of various gas-turbine-engine designs. The basis for this methodology is a combination of turbine-disk and low-cycle-fatigue methodologies that was developed in pioneering work published during the years 1947 through 1965. The present methodology goes beyond the previous methodology in that its structural-analysis component is built on an enhanced mathematical model of a rotating turbine disk and is integrated with an optimization component.

In the previous methodology, the mathematical model of a turbine disk was one of constant thickness. In the present methodology, the thickness of the disk can vary with radius in piecewise-linear fashion; in addition, the temperature gradient in the disk is also modeled as a piecewise-linear function of radius. The differential equations of radial and tangential components of stress and strain in the disk are formulated under some straightforward simplifying assumptions (e.g., thickness \ll radius at all points of interest, and the disk material obeys Hooke's law and is homogeneous and isotropic). The equations are solved numerically by a finite-difference technique.

The incorporation of an optimization procedure saves much time, inasmuch as iterations that would otherwise have to be initiated manually are initiated and completed automatically by a computer. The time saved can be as much as 3 weeks per rotating disk. In this program, the optimization takes no more than 5 minutes. The optimization is performed by the sequence-of-unconstrained-minimizations (SUMT) technique, which is widely used for solving minimization



Structural-Analysis and Optimization Procedures are performed by several computer programs that act in conjunction, in response to data acquired from the flow-path-analysis program WATE.

problems that involve linear and nonlinear constraints or unconstrained functions. In this case, the objective function that one seeks to minimize is the mass of the disk, while the constraints pertain to maximum allowable levels of stress and relationships among the radii where the slope of the thickness-vs.-radius function changes. The optimization procedure can be summarized as follows:

1. Calculate the loads, stresses, and strains for an initial disk geometry that is based

on the chord length of the turbine blades and the radii of the shaft and flow path.

2. Given the geometry and loads calculated, evaluate the constraints.
3. Upon violation of any of the constraints, modify the disk geometry until all constraint equations are satisfied and the mass of the disk is a minimum.

The structural-analysis and optimization components of the methodology are implemented in a computer program, along with a low-cycle-fatigue component adopted from the previous methodology. This program is executed in conjunction with an interface computer program that gathers needed data from a flow-path-analysis program called "WATE" (see figure). The combination of programs requires minimal intervention by the user, and can be used as a postprocessor of the WATE output.

In a test case involving a tenth-stage compressor disk, the stress-analysis portion of the methodology and computer program were assessed by comparing the computed stresses and displacements with those predicted in a finite-element analysis; the two sets of predictions agreed within 3 percent. In a test of the optimization component of the methodology, the mass of the rotating compressor disks was reduced by 26 percent from the initial design mass.

This work was done by Susan C. Armand of Lewis Research Center. Further information is contained in a TSP (see page 1).

Inquiries concerning rights for the commercial use of this invention should be addressed to NASA Lewis Research Center, Commercial Technology Office, Attn: Tech Brief Patent Status, Mail Stop 7-3, 21000 Brookpark Road, Cleveland, Ohio 44135. Refer to LEW-16422.

Biomimetic Explorers

Exploratory robots would feature animal-like adaptability and mobility.

"Biomimetic explorers" are a class of proposed small robots that would be equipped with microsensors and would feature animal-like adaptability and mobility. These robots would capture key features, a specific design or function found in

nature, taking advantage of general animal mechanical designs and neural functions that have evolved to enable animals to move through various environments. These robots are conceived for use in remote, hostile, and/or inaccessible ter-

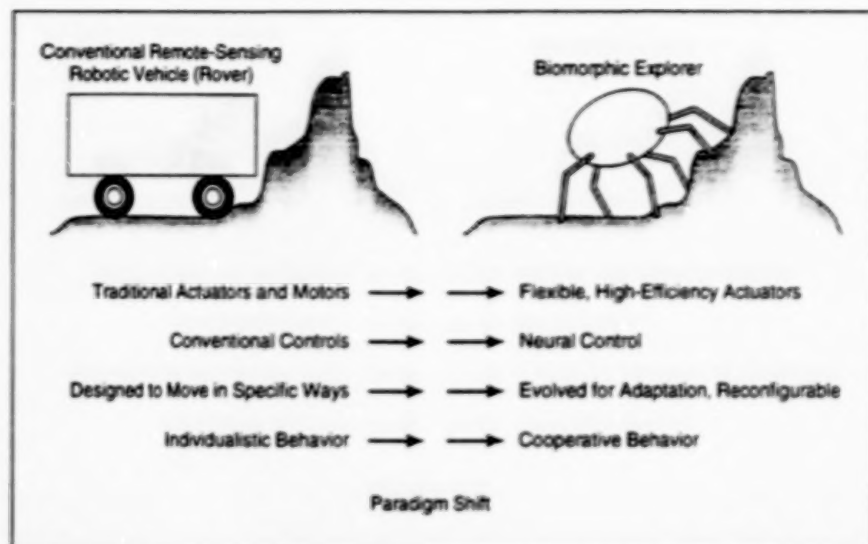
NASA's Jet Propulsion Laboratory, Pasadena, California

trial and other planetary environments, where they would be used to perform such diverse functions as acquisition of scientific data, law-enforcement surveillance, or diagnosis for precise, minimally invasive medical treatment. Depending on

the specific environment to be explored, a biomorphic explorer might be designed to crawl, hop, slither, burrow, swim, or fly.

The biomorphic-explorer concept is a generalization and encompasses the nanorover concept reported in "Tetherless, Optically Controlled Nanorovers" (NPO-19606), *NASA Tech Briefs*, Vol. 21, No. 3 (March 1997), page 92. Like nanrovers, biomorphic explorers would exploit the emerging technology of microelectromechanical structures. Biomorphic explorers would be enabled by a unique combination of direct-driven, flexible, shape-reconfigurable advanced actuators and their adaptive control by fault-tolerant biomimetic algorithms. Typically, these actuators would consist largely of composites of thin piezoceramic films on strong polymeric substrates and/or combinations of shape-memory-alloy actuators. The actuators would generate forces and/or displacements in response to light or to applied voltage; that is, they could be controlled photonically or electronically. The desired combinations of mobility and adaptability, along with fault tolerance and a limited capability for "learning," would be achieved by integrating the actuators with very-large-scale integrated (VLSI) circuits that would implement neural-networks utilizing genetic algorithms.

Relative to conventional remote-sensing robotic vehicles, biomorphic explorers would be simple, inexpensive, and easy to fabricate; this raises the possibil-



The Development of Biomorphic Explorers would be consistent with a current trend away from conventional, limited-mobility robots toward highly mobile, adaptive robots based partly on biological concepts.

ity of mass production of expendable biomorphic explorers that could be deployed in large numbers, possibly acting cooperatively under central control or distributed control. Such deployment would, of course, resemble the behavior of colonies of insects or other groups of small social animals engaged in cooperative activity.

This work was done by Santa Thakoor and Adrian Stoica of Caltech for NASA's Jet Propulsion Laboratory. Further information is contained in a TSP [see page 1].

In accordance with Public Law 96-

517, the contractor has elected to retain title to this invention. Inquiries concerning rights for its commercial use should be addressed to

Technology Reporting Office
JPL
Mail Stop 122-116
4800 Oak Grove Drive
Pasadena, CA 91109
(818) 354-2240

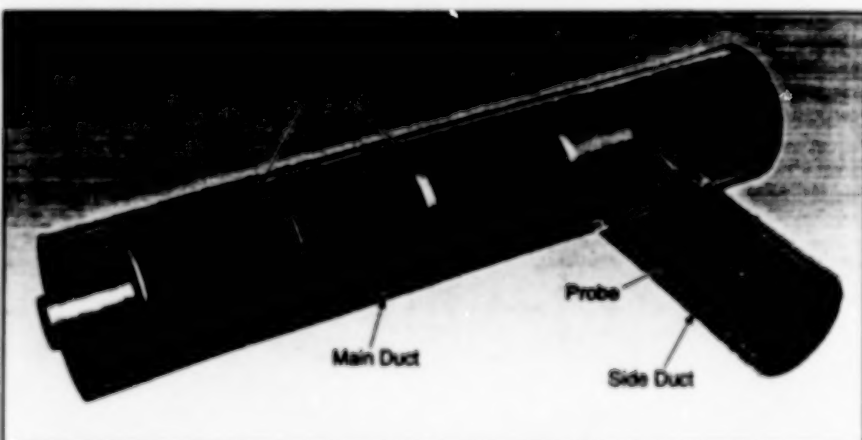
Refer to NPO-20142, volume and number of this NASA Tech Briefs issue, and the page number.

Walking Robot for Internal Inspection of Thin-Wall Ducts

Inflated bladders would provide gentle support with tolerance for misalignment.

John F. Kennedy Space Center,
Florida

A walking robot connected to external instrumentation via a tether has been proposed to enable visual inspections, retrieval of loose objects, and some repairs inside thin-wall round ducts. The ducts in question are made of sections about 4 ft (1.2 m) long, joined by flexible seals that accommodate axial gaps and lateral misalignments of as much as 1/4 in. (6 mm) between sections. The sections can be oriented horizontally or vertically. Some duct sections include, variously, changes in diameter, bends, and openings into side ducts. The robot is required to negotiate all such sections at distances up to 60 ft (18.3 m) from the point of entry, without damaging the thin duct walls. The robot is required to be



Bladders Would Be Inflated to support the robot gently within the main duct. In addition to enabling visual inspection of the interior of the main duct, the robot could extend a probe for inspection of an adjacent portion of a side duct.

able to enter a duct through an opening as small as 4.5 in. (11.4 cm) and to move along the duct.

To prevent damage, the load exerted by the robot at a location of contact with a duct wall must be limited to 2.5 psi (17 kPa) or less. The total weight of the robot (including repair and retrieval tools and inspection video cameras but excluding the tether, tether reel, and external instrumentation) must be less than 20 lb (9 kg). The tether [61 ft (18.6 m) long] must weigh less than 10 lb (4.5 kg).

The basic requirements for gentle support, tolerance of misalignment between sections, and ability to accommodate bends would be satisfied by use of bladders that would be inflated after the robot had been placed inside the duct (see figure).

The inflation pressure would be just enough to support the robot approximately centrally within the duct and to generate sufficient friction between the bladders and the duct wall to keep the robot from sliding along the duct wall when motion was not desired.

The robot would walk in a quasi-inch-worm fashion by a combination of electrical and mechanical actuation, which would include alternate inflation and deflation of the fore and aft bladders in coordination with alternate lengthening and shortening of the structure between the bladders. Moreover, the inflation of both bladders during a stop would orient the axis of the robot approximately along the local duct axis, thereby providing a directional reference for interpretation of images from the cameras.

This work was done by Dimitrios Apostolopoulos and Warren C. Whittaker of RedZone Robotics, Inc., for Kennedy Space Center.

In accordance with Public Law 96-517, the contractor has elected to retain title to this invention. Inquiries concerning rights for its commercial use should be addressed to

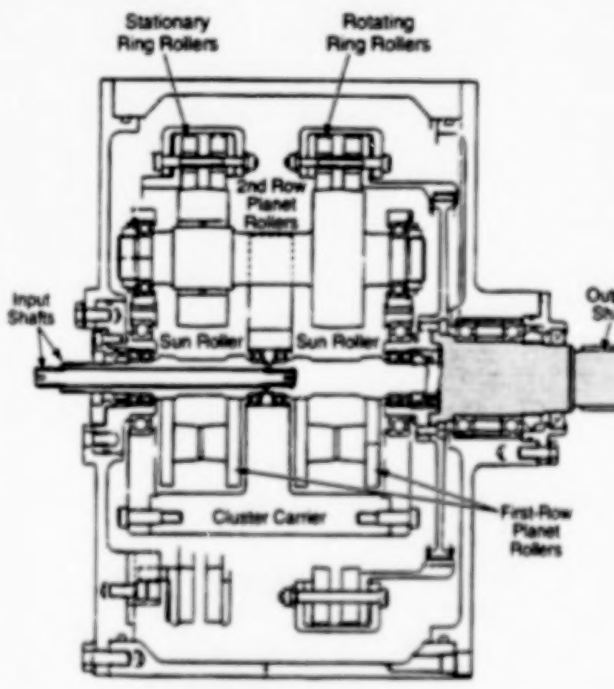
David White,
VP Business Development
RedZone Robotics, Inc.
2425 Liberty Ave.
Pittsburgh, PA 15222-4639
(412) 765-3064

Refer to KSC-12001, volume and number of this NASA Tech Briefs issue, and the page number.

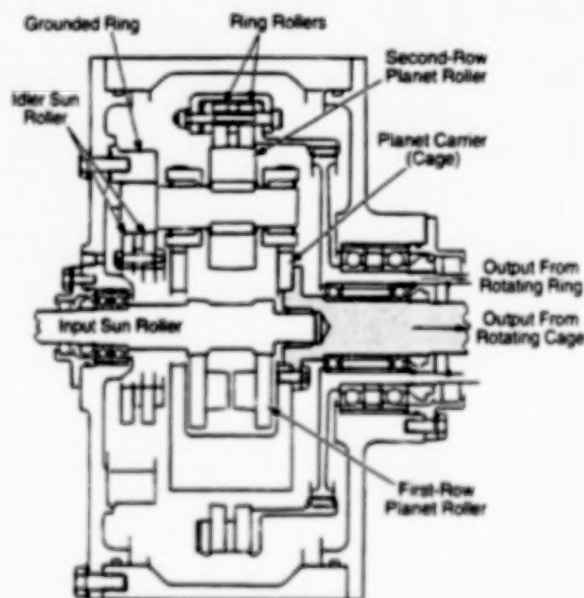
Improved Roller and Gear Drives for Robots and Vehicles

One type is designed to eliminate stick/slip, another to eliminate reaction torque.

Lewis Research Center,
Cleveland, Ohio



DIFFERENTIAL DRIVE



ANGULAR-MOMENTUM-BALANCED DRIVE

These Improved Gear Drives offer advantages for control of traction and rotary actuation in robots. In addition, drives of the differential type could be used in variable-speed transmissions in automobiles.

Two types of gear drives have been devised to improve the performances of robotic mechanisms. One type features a dual-input/single-output differential-drive configuration intended to eliminate stick/slip motions; the other type features a single-input/dual-angular-momentum-balanced-output configura-

tion intended to eliminate reaction torques.

Stick/slip motion can degrade the performance of a robot because a robotic control system cannot instantaneously correct for a sudden change between static and dynamic friction. Reaction torque arises in a structure that supports a mecha-

nism coupled to a conventional gear drive, and can adversely affect the structure, the mechanism, or other equipment connected to the structure or mechanism.

In a drive of the differential type, the two input shafts can be turned at different speeds and, if necessary, in opposite directions, to make the output shaft

turn in the forward or reverse direction at a desired speed. This is done without stopping rotation of either input shaft, so that stick/slip does not occur. In a drive of the angular-momentum-balanced type, turning the single input shaft causes the two output shafts to rotate at equal speeds in opposite directions.

The figure schematically illustrates one of two drives of the differential type and one drive of the angular-momentum-balanced type that have been built and tested. Each of the differential drives is rated at input speeds up to 295 radians per second (2,800 r/min), output torque up to 450 N·m (4,000 lb-in.), and power up to 5.6 kW (7.5 hp). The maximum ratings of the angular-momentum-balanced drive are input speed of 302 radians per second (2,880 r/min), dual output torques of 434 N·m (3,840 lb-in.) each, and power of 10.9 kW (14.6 hp).

Each differential drive features either (as explained in the next two sentences) a dual roller-gear or a roller arrangement with a sun gear, four first-row planet gears, four second-row planet gears, and a ring gear.

One of the differential drives contains a planetary roller-gear system with a reduction ratio (measured with one input driving the output while the other input shaft remains stationary) of 29.23:1. The other differential drive (the one shown in the figure) contains a planetary roller system with a reduction ratio of 24:1. The angular-momentum-balanced drive features a planetary roller system with five first- and second-row planet gears and a reduction ratio (the input to each of the two outputs) of 24:1. The three drives were subjected to a broad spectrum of tests to measure linearity, cogging, friction, and efficiency. All three drives operated as expected kinematically, exhibiting efficiencies as high as 95 percent.

Drives of the angular-momentum-balanced type could provide a reaction-free actuation when applied with proper combinations of torques and inertias coupled to output shafts. Drives of the differential type could provide improvements over present robotic transmissions for applications in which there are requirements for extremely smooth and accurate torque

and position control, without inaccuracies that accompany stick/slip. Drives of the differential type could also offer viable alternatives to variable-ratio transmissions in applications in which output shafts are required to be driven both forward and in reverse, with an intervening stop. A differential transmission with two input drive motors could be augmented by a control system to optimize input speeds for any requested output speed; such a transmission could be useful in an electric car.

This work was done by William J. Anderson and William Shipton of Nastec, Inc., and Wyatt Newman of Case Western Reserve University for **Lewis Research Center**. Further information is contained in a TSP [see page 1].

Inquiries concerning rights for the commercial use of this invention should be addressed to NASA Lewis Research Center, Commercial Technology Office, Attn: Tech Brief Patent Status, Mail Stop 7-3, 21000 Brookpark Road, Cleveland, Ohio 44135. Refer to LEW-16290.

BLANK PAGE



Mathematics and Information Sciences

Hardware, Techniques, and Processes

53	Robust Aeroservoelastic-Stability Margins
54	Algorithm for Initialization of a Convolutional Decoder
55	Improved Parallel Computation of Electromagnetic Scattering
57	Converting Particle-Fallout Data to Obscuration Levels

BLANK PAGE

Robust Aeroservoelastic-Stability Margins

Structural dynamics of the closed-loop system are analyzed.

Dryden Flight Research Center,
Edwards, California

In aeroservoelastic (ASE)-stability analysis, one considers the coupling of the aerodynamic, inertial, structural, actuation, and control-system elements of the dynamics of an aircraft. The closed-loop interactions of these elements can introduce unexpected instabilities in flight if the analytical model used for synthesis and analysis is not accurate. Measures of allowable flight-condition variations, called "stability margins," should be computed to indicate the range of velocities and attitudes within which the aircraft can safely operate.

An approach known as the μ method was recently introduced for analyzing stability margins of open-loop flexible aircraft models. [The μ method was described in "Characterizing Worst-Case Flutter Margins From Flight Data" (DRC-97-03), NASA Tech Briefs, Vol. 21, No. 4 (April 1997), page 62.] This method is based on a formal mathematical concept of robustness that guarantees a level of modeling errors to which the aircraft is robustly stable. A realistic representation of errors can be formulated by describing differences between predicted responses and measured flight data. The structured singular value, μ , is used to compute a margin that is robust to these errors.

The μ method has now been extended to enable the evaluation of aeroservoelastic-stability margins of closed-loop, flexible aircraft models. For a given aircraft, uncertainty operators are introduced into the analysis to describe errors in the structural and aerodynamical models along with errors in the sensor and actuator models. The resulting stability margins are superior to such traditional measures as gain and phase margins, which cannot be easily interpreted as flight-condition information. Also, the extended μ method can be used to simultaneously compute closed-loop ASE stability margins and open-loop flutter stability margins.

Flight data are easily incorporated into the stability analysis in this method. Uncertainty operators are derived by model validation to ensure that the dynamics observed in the data are represented in a robust mathematical model. The stability-margin parameter, μ , is robust to the measured variations associated with the uncertainty operators. In this sense, the stability margins are worst-case

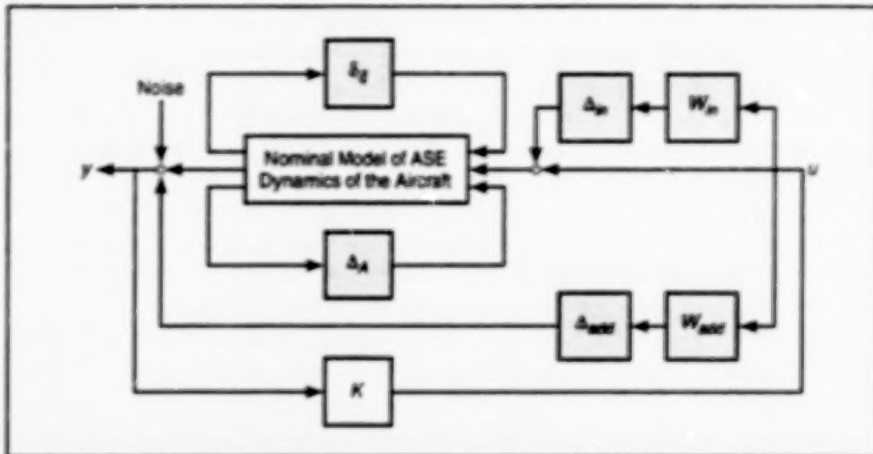


Figure 1. The Uncertainty Operators described in the text are incorporated into the mathematical model along with the nominal dynamical model of the aircraft, with a feedback-control gain matrix K , and with uncertainty-weighting operators W_{out} and W_{in} .

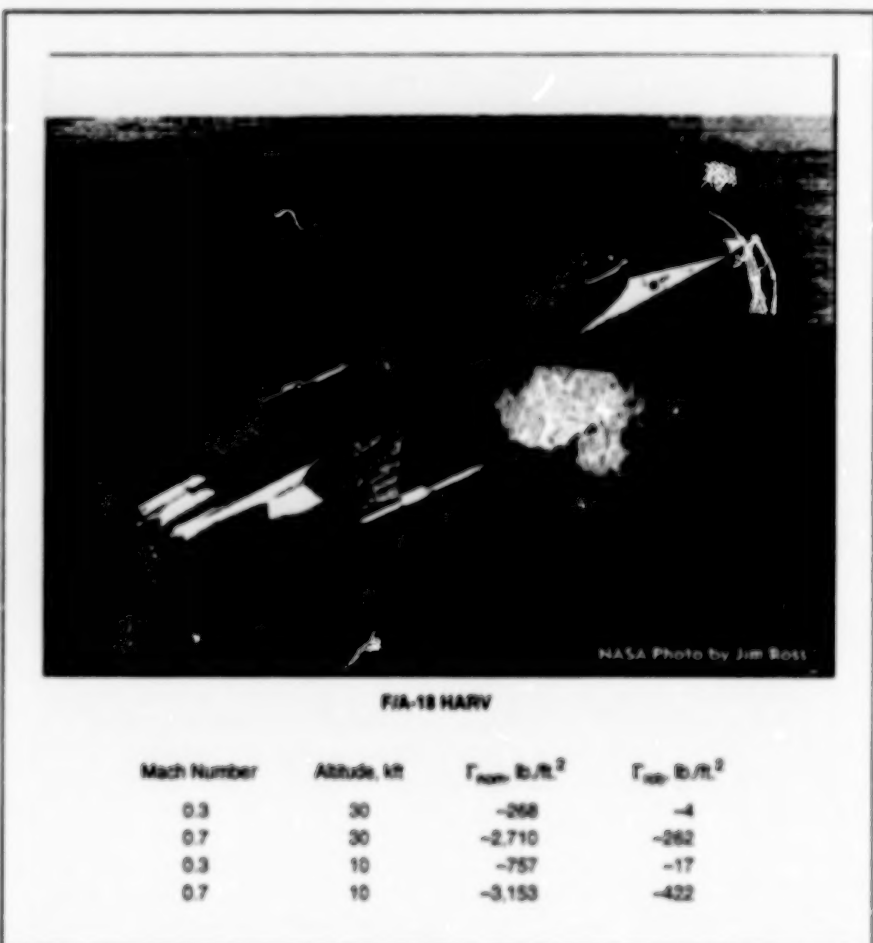


Figure 2. Nominal and Robust Stability Margins — Γ_{nom} and Γ_{rob} , respectively — were calculated for closed-loop operation of the F/A-18 HARV equipped with a thrust-vectoring control subsystem.

margins with respect to the flight data.

In the extended μ method, an uncertainty description, as shown in Figure 1, is formulated for the mathematical model of a given aircraft. This description includes Δ_A to account for errors in the modal parameters, of the state matrix, Δ_h to account for multiplicative errors in the actuator models, and Δ_{add} to account for remaining errors and unmodeled dynamics. An additional operator, $\delta_{\bar{\zeta}}$ is included to represent variations in flight condition and ensure the model is robust to all variations less than the stability margin. Magnitudes of the uncertainty operators are computed to account for errors observed between predicted responses of the model and measured flight data from accelerometers.

In an application of the foregoing methodology, ASE-stability margins were computed for the F/A-18 High Alpha Research Vehicle (HARV). There had been concern about the closed-loop stability margins of this aircraft operating with high angles of attack at high altitudes. The ASE stability margins are given in Figure 2 for the aircraft model at the extreme ranges of flight conditions in which the HARV operates. These margins are the biggest decreases in dynamic pressures that may be safely considered before an ASE instability can be encountered. The parameters Γ_{nom} are the stability margins computed without consideration of any modeling errors or uncertainties. These margins indicate that the nearest unstable

flight condition for the nominal model is quite far from the flight envelope. The parameters Γ_{rob} are the stability margins computed with consideration for errors and uncertainties. These margins are considerably smaller than the nominal margins and indicate that the nearest instability may actually lie quite close to the flight envelope. In particular, the model at mach 0.3 and altitude of 30,000 ft (9.1 km) has very little robustness to the errors that are observed from the flight data.

This work was done by Martin Senneter of Dryden Flight Research Center and Rick Lind of NRC. Further information is contained in a TSP [see page 1].
DFC-98-37

Algorithm for initialization of a Convolutional Decoder

The decoder can be initialized "on the fly."

NASA's Jet Propulsion Laboratory,
Pasadena, California

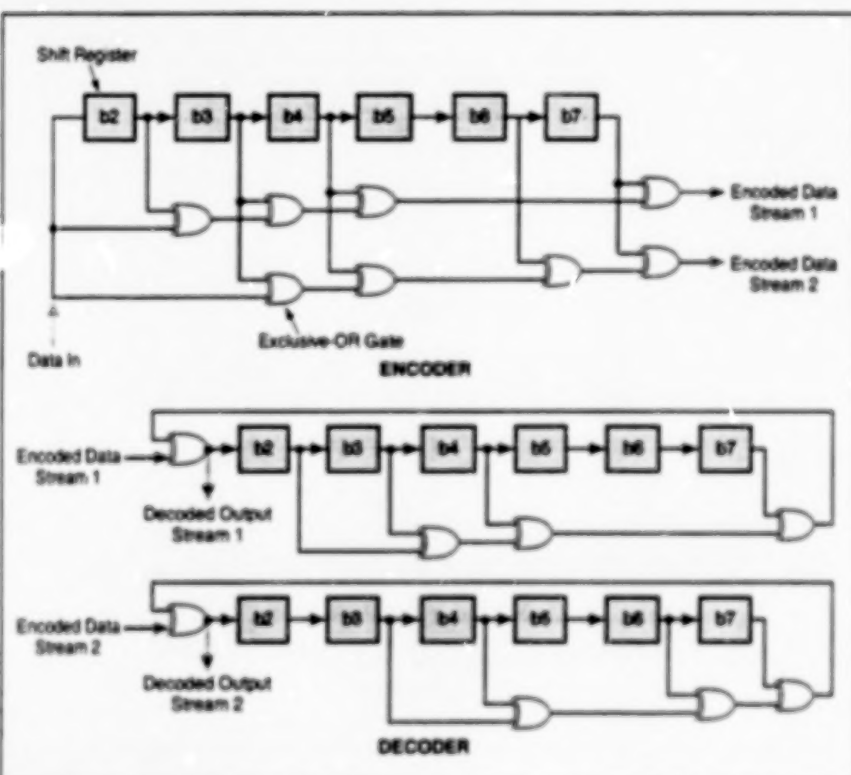


Figure 1. Shift Registers and Exclusive-OR Gates implement the digital logic for encoding and decoding in a convolutional code of length $7^{1/2}$.

An algorithm effects rapid initialization of a convolutional decoder. This algorithm can be applied "on the fly"; that is while the decoder is receiving a stream of convolutionally encoded data. In comparison with other means of initialization, this algorithm is simpler, and it can be embedded in decoder hardware at relatively low cost.

"initialization" in this context denotes

establishment of the correct initial code state of the decoder. Standard convolutional decoding requires setting the decoder in a known initial state consistent with the state of the encoder; without initialization, the decoder cannot reconstruct the original uncoded data stream.

The algorithm is best described via the example illustrated in Figure 1, which

shows the logic diagram of a coder-decoder pair that implements a binary convolutional code of length $7\frac{1}{2}$. The encoder processes the input data stream into two encoded data streams. A notable property of convolutional encoding is that the initial state of the encoder determines the encoder outputs. In this case, there are 2^6 possible initial states, and it is therefore reasonable to assume that an input data stream could be mapped to any one of as many as 2^6 unique pairs of encoded data streams. In a typical application, the encoder registers are preloaded with some known bit pattern to restrict the encoder to one of the 2^6 possibilities.

The algorithm is based on the discovery that the pattern used to initialize the decoder can be calculated in real-time from the encoded data. The two encoded data streams are fed to two input terminals of the decoder, which processes these streams to produce two output streams. Provided that the decoder is initialized by use of the same bit pattern that was preloaded into the decoder, both output bit streams are forced to remain the same during the first six decoder shift cycles. Thereafter, if the decoder has been initialized correctly, both output streams should continue to be identical and to contain the original data in uncoded form. If the decoder has not been initialized correctly, then typically the decoder output bit streams begin to differ.

The algorithm (see Figure 2) can be started at any time during reception of the encoded data streams. From the first six

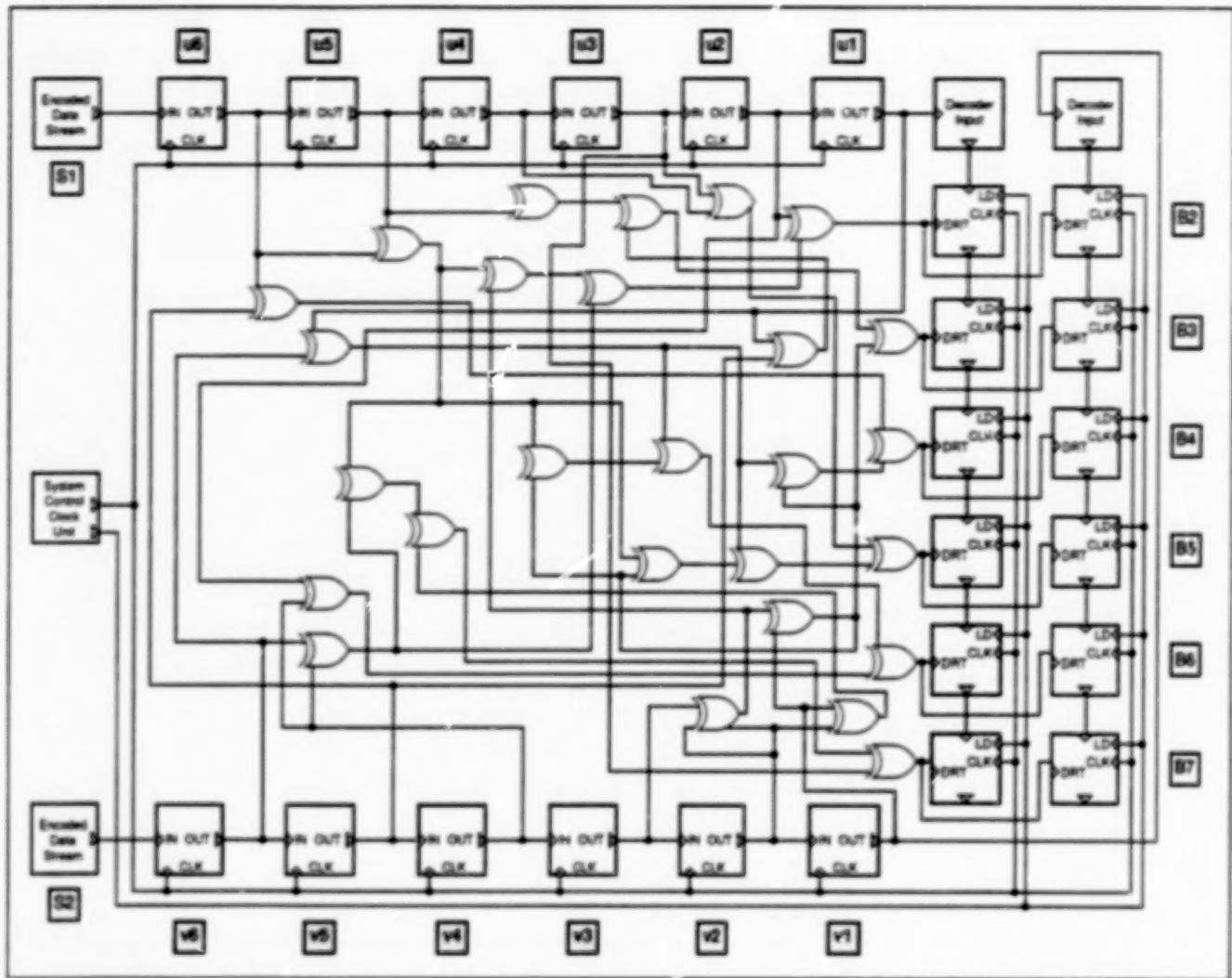


Figure 2. The Initialization Algorithm can easily be implemented in hardware.

pairs of encoded bits following its start, the algorithm calculates what the initial state of the decoder should have been, then it tests the calculated initial state for alignment of the two decoder output streams as described above. If the calculation of the initial decoder state has been success-

ful, the decoder is synchronized and the algorithm is terminated. If the calculation has not been successful, then the alignment of the encoded data streams at the input of the decoder is shifted and another decoding run is made in the effort to achieve synchronization. This procedure is

repeated until synchronization is achieved or until an error is detected.

This work was done by Frank M. Loya of Caltech for NASA's Jet Propulsion Laboratory. Further information is contained in a TSP [see page 1]. NPO-19776

Improved Parallel Computation of Electromagnetic Scattering

Solutions can be computed on unstructured grids, without need for traditional mesh-partitioning algorithms.

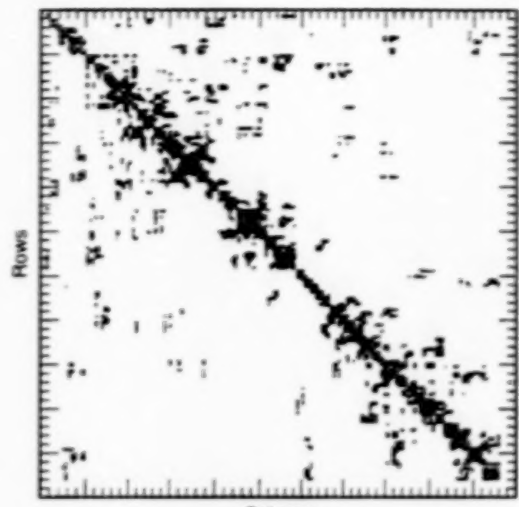
An improved method of parallel computation of the electromagnetic-scattering characteristics of complexly shaped objects has been devised. This method belongs to a class of methods that involve the finite-element solution of Maxwell's equations on unstructured grids. ("Unstructured grids" in this context does not signify grids that lack structure; instead, it is a specialized term for grids with arbitrarily specified,

complex, and/or irregular structures.) As explained below, the present method effects a simplification (relative to the older methods in the same class) in the use of parallel computers, and involves an algorithm that is scalable in the sense that it is readily useable on large, massively parallel computers.

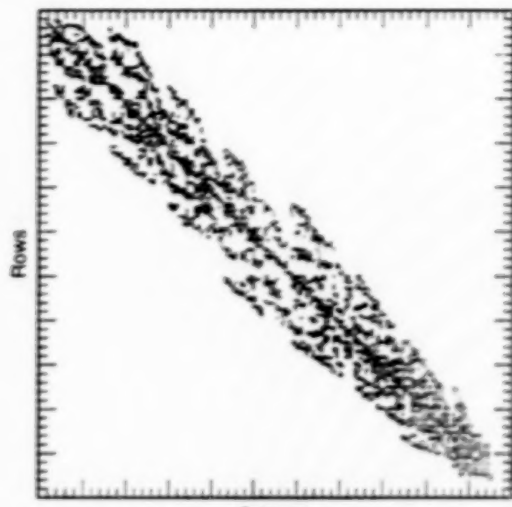
A finite-element mathematical model is needed to represent a typical electromagnetic-scattering structure that

NASA's Jet Propulsion Laboratory,
Pasadena, California

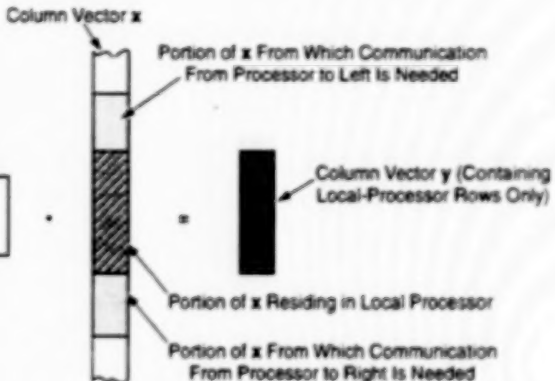
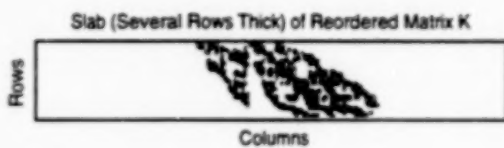
includes components made of various electromagnetically penetrable (e.g., dielectric) and/or impenetrable (electrically conductive) materials. An unstructured grid is needed to represent the complexity of the geometry of such a structure and its components. In the present method as in the other methods of the same class, the computational grid or mesh for a given problem must be truncated at a surface that surrounds



ORIGINAL MATRIX



REORDERED MATRIX



ROW-SLAB DECOMPOSITION AND MATRIX-VECTOR MULTIPLICATION

The Nonzero Elements of the Sparse Matrix are indicated by the colored spots. The matrix is reordered for minimum bandwidth, then subjected to the row-slab decomposition to enhance the efficiency of the parallel computation of the matrix-vector product $Kx = y$.

the scattering structure at a suitable distance. The surface must be chosen consistently with the need to both maintain accuracy of the computed electromagnetic field and limit the meshed volume of free space. Maxwell's equations for the electromagnetic field are put in three-dimensional Helmholtz wave-equation form and solved on the mesh by a coupled finite-element/integral-equation technique.

The specific integral-equation formulation is of a boundary-element type. This formulation results in efficient and accurate truncation of the computational domain. A system of equations in partitioned-matrix-partitioned-vector form results from the combination of (1) finite-element discretization of the volume in and around the scattering structure and (2) integral-equation discretization of the surface. The system of equations is solved by a combination of (1) an iterative sparse-matrix-

equation-solving subalgorithm and (2) a dense-matrix-factorization subalgorithm. The assembly and solution of the matrix equation and the computation of observable quantities are all accomplished in parallel, using various numbers of processors at various stages of the calculation.

A common feature of the older methods is the need for mesh-partitioning algorithms to distribute the unstructured mesh and the sparse matrix entries among the available processors. This need arises from the distributed-memory architecture of typical parallel computers and the consequent lack of direct access, by every processor, to all the mesh and matrix data. In the present method, one does not explicitly partition the mesh; instead, one emphasizes decomposition of the sparse matrix entries among the processors, and such mesh partitioning as happens to occur becomes merely incidental to this

decomposition. The choice of a specific decomposition is guided by recognition that what one needs to compute efficiently at each step of the iterative subalgorithm is the inner product of a sparse matrix and a dense vector.

The chosen decomposition is of a row-slab type. The figure illustrates aspects of the row-slab decomposition for an example problem. The top left part of the figure shows the original structure of the sparse matrix. The top right part of the figure shows the structure of the matrix as reordered for minimum bandwidth in preparation for the row-slab decomposition and the resulting matrix-vector multiplication $Kx = y$. Each processor handles one slab. Because of the minimum-bandwidth reordering, the minimum and maximum column indices of each slab are known. If the row indices of that piece of the dense vector x that is local to this

processor contain the range from the minimum to the maximum column index for this slab, then the multiplication can be done purely locally, and the corresponding part of the product vector y will be purely local. In general, the column indices range beyond the local row indices; this gives rise to a need for a communication step to obtain the adjacent portions of x that are not local to

this processor. This communication step involves data from a few processors to the left and right. The number of processors communicating data depends on the row bandwidth of the slab and the number of processors in use. Overall, the row-slab decomposition strikes a balance among (1) nearly perfect balance of data and computational load among processors, (2) minimal albeit

suboptimal communication of data in the matrix-vector multiplication, and (3) scalability to larger problems on greater numbers of processors.

This work was done by Tom Cwik, Cinzia Zuffada, and Vahraz Jamnejad of Caltech for NASA's Jet Propulsion Laboratory. Further information is contained in a TSP [see page 1].

NPO-20171

Converting Particle-Fallout Data to Obscuration Levels

A worksheet has been constructed within the Microsoft Excel software system for converting raw particle-fallout data into percentages of obscuration; that is, percentages of areas obscured by particles on surfaces. These obscuration levels are needed for assessing contamination levels in nominally clean manufacturing and assembly facilities. The raw data are obtained by an automated instrument that scans witness plates, determines the sizes of particles that have fallen onto the plates

by analyzing their light-scattering characteristics, and counts the number of particles in each of six size ranges. For a given witness plate, the user enters the number of particles counted in each size range into a designated space on the worksheet. Within each size range, the unknown particle-size distribution is assumed to be characterized by a log-normal slope represented by a line that connects the cumulative counts at the limits of the size ranges. The worksheet software uses the

counts and this assumed distribution to compute an overall particle-size distribution, which is then used to compute the percent obscuration.

This work was done by Christian J. Schwindt formerly of I-Net and Eugene N. Borson of Swales & Associates, Inc., for Kennedy Space Center. Further information is contained in a TSP [see page 1]. KSC-11956

National Aeronautics and
Space Administration



END

12\09\98